Composite Structures 310 (2023) 116705

Contents lists available at ScienceDirect

Composite Structures

journal homepage: www.elsevier.com/locate/compstruct

Modelling and design of hierarchical fibre-graphene nanoplatelets reinforced elasto-viscoplastic polymer matrix composites to improve crashworthiness and energy absorption

Ahmed Elmasry [a,*], Wiyao Azoti [b], Ahmed Elmarakbi [a]

[a] Faculty of Engineering and Environment, Northumbria University, Newcastle upon Tyne NE1.8ST, UK
[b] Clément Ader Institute (ICA), Federal University Toulouse Midi-Pyrénées, UMR CNRS 5312, INSA, ISAE-SUPAERO, IMT Mines Albi, UPS, 3 rue Caroline Aigle, 31400 Toulouse, France

ARTICLE INFO

Keywords:
Graphene nanoplatelets
Polymer matrix composites
Multi-site modelling
Thermo elastic–viscoplasticity
Micromechanics
RVE
FE modelling

ABSTRACT

Today, light-weighting for energy efficiency without sacrificing safety and performance attributes has become a primary focus in the automotive industry. In the field of modelling graphene nanocomposites' structural applications under severe loading conditions, literature is limited. In addition, the existing work only employs the so-called one-site (OS) modelling. This study develops an approach to study 3-phases hierarchical fibres/graphene nanoplatelets (GNPs)-reinforced polymer matrix composites utilising OS modelling and what is known as multi-site (MS) modelling. The MS modelling accounts for material anisotropy considering the interaction between neighbouring inclusions. Applicability of both models is then assessed for automotive components' crashworthiness response under combined mechanical and rate-dependent plasticity or viscoplasticity behaviours. A coherent micromechanical design is employed with elastic platelets and elasto-viscoplastic matrix assumptions. The micromechanics modelling combines rate-dependent constitutive laws and thermomechanical properties for the nonlinear response of composite materials. The heterogeneous material problem is resolved in the first instance for a thermoelastic case. The thermomechanical kinematic integral equation is used to derive the strain concentration tensor. Using the generalised Mori–Tanaka (GMT) homogenisation scheme, effective thermomechanical properties are obtained. For the nonlinear behaviour, a linearisation of the classical J_2 rate-dependent model is considered with an isotropic hardening. Based on an implicit integration scheme, a consistent tangent modulus is obtained and serves as a uniform modulus for homogenisation of the rate-dependent thermomechanical composite material. An application is therefore performed on a short glass -fibres/graphene nanoplatelet/ Polyamide-Nylon 6 (GNP/PA6) composite. The current study's archival value is to provide an auspicious approach for a consistent design and application of this category of materials for automotive structural components.

1. Introduction

Improving fuel efficiency and vehicle performance lies with decreasing the weight of vehicle components while at the same time maintaining safety [1,2,3]. Reinforced polymer composites are among widely preferred form of composite that has been used for light-weighting in the automotive industry. They offer superior properties such as impact strength, easy moldability, improved aesthetics, and reduced weight compared to conventional automotive components [4,5,6,7]. However, polymer composites are susceptible to environmental factors such as temperature, time, exposure to liquids, gases, electrical fields, and radiation, which cause polymer composites' properties degradation and consequently decrease their performance [8,9].

In the realm of nanotechnology and two-dimensional materials, graphene continues to thrive on the horizon of materials science. With theoretical and experimental results on individual graphene nanosheets exhibit incredibly high values of Young's modulus (~1000 GPa) [10,11,12], adding graphene at lower volume fractions as a reinforcement to polymers or fibre-reinforced composites offers substantial property enhancements for lightweight components including enhancing strength, durability, flexibility, thermal and electrical conductivity [13,14,15]. Thus, the study of graphene-based composites is a

* Corresponding author.
E-mail address: ahmed.elmasry@northumbria.ac.uk (A. Elmasry).

https://doi.org/10.1016/j.compstruct.2023.116705
Received 14 July 2022; Received in revised form 29 November 2022; Accepted 13 January 2023
Available online 20 January 2023

strategic objective for developing new lightweight and multifunctional structures for the automotive sector [16,17,18] with huge potentials for structural applications in the automotive industry. However, implementing graphene composites on commercial high-performance structural applications under severe loading conditions, such as automotive structural components, has been in immature stages requiring further investigation.

Modelling materials, predicting their behaviour under different conditions, and developing/designing cost-effective materials with improved or required properties are prime objectives in materials research and industry. Today, computational materials science has progressed to be realistic and become an essential paramount predictive tool for exploring materials' properties and behaviour and understanding complex physical phenomena observed in materials [19,20,21,22]. Moreover, the mechanical behaviour of real materials is, essentially, rate- or time-dependent plasticity (or viscoplasticity). For example, the strain increase with increasing time under constant load, i.e. creep phenomenon. In general, viscoplasticity or creep importance in materials escalates with increasing temperature. Thus, comprehensive analytical methods are required to accurately predict this nonlinear, time-dependent behaviour.

In addition, composite materials exhibit anisotropy resulting from their microstructure. The anisotropy of mechanical properties relies on topological texture, i.e. the orientation and spatial distribution of the reinforcement. Besides, the morphological texture, referred to as the aspect ratio also plays an important role in the response of the composite. The accuracy of predictive models resides in accounting for the interaction between inclusions and their surrounding neighbourhood. This approach, called the multi-site (MS) modelling [23,24], was first developed by Fassi-Ferhi [25] for local fields of pairwise heterogeneous and plastic inclusions embedded in an anisotropic matrix.

However, most existing work only employs a simpler approach called one-site (OS) modelling, which ignores particle interactions. Other research works dealing with the pairwise particle-interaction through micromechanics formulation have been done by Ju and Chen [26,27] for spherical inclusions, by Ju and Tseng [28] for randomly dispersed elastoplastic phases and by Ju and Sun [29], and Sun and Ju [30] for randomly located and aligned spheroidal inclusions.

The MS modelling was used more recently by Kpobie et al. [31] to derive the thermoelastic properties of anisotropic cubic composites. The framework of the MS modelling is used by Azoti et al. [32] to derive the macroscopic response of elastoplastic composites with ordered microstructures.

Several multiscale modelling methods exist to derive the effective properties of a heterogeneous medium utilising homogenisation [33] of the fundamental physical properties of its constituents or vice versa [24,34]. For example, Pineda et al. [35] utilised the "generalized method of cells" model to capture progressive failure within the constituents of a unidirectional fibre-reinforced composite material. Kaleel et al. [36] proposed a simplified version of the classical FE^2 concurrent multiscale method for composite materials to save computational costs. Sun et al. [37] presented a micromechanical interphase model to investigate the influence of interface effects on the elastoplastic behaviour of graphene-reinforced nanocomposites.

In view of the importance of having a thermal effect in the effective behaviour properties; Tsiamaki et al. [38] and Tsiamaki and Anifantis [39] numerically investigated the thermomechanical properties of graphene nanocomposites and reported that the temperature increase and the multiplicity of graphene layers lead to a decrease of the mechanical properties. Sandu [40] and Yang et al. [41] investigated the thermal conductivity of graphene-based nanocomposites and reported higher results than that of the matrix material. Rahman et al. [42], Zhao et al. [43], Zhou et al. [44], Pinto et al. [45], Wang et al. [46], and Tarawneh et al. [47] experimented with graphene to enhance the thermomechanical properties of composite materials and reported improvement over the matrix material. Georgantzinos et al. [48] utilised a spring-based finite element (FE) approach to predict the thermomechanical behaviour of graphene. Li et al. [49] studied the nonlinear thermal performance of the functionally graded porous cylinder with the graphene nanofillers embedded in elastic matrix.

Our current work accounts for composite viscoplasticity using a rate-dependent thermomechanical model considering polymeric matrix. In the case of thermoplastic matrix, the stress–strain response depends on the strain rate both below and above the yield stress, i.e. viscoplastic constitutive models [50]. The material anisotropy is accounted for by the interaction of the inclusion and a defined neighbourhood using the MS modelling. Using the generalised Mori–Tanaka (GMT) homogenisation scheme, effective thermomechanical properties are obtained. The non-linear behavioural response is established in the framework of the J_2 flow rule model is considered with an isotropic hardening. Numerical characterisations involving tensile and compression tests of short glass fibres/graphene nanoplatelet/ Polyamide-Nylon 6 (E-Glass/GNP/PA6) composite enable the determination of damage and failure thresholds for crashworthiness applications. Modelling of symmetric crush tube of an automotive crash-box demonstrates the crash performance characterised by the peak crash force, absorbed energy and specific energy absorption (SEA) [51]. The current research provides a promising straightforward approach to a consistent material design for graphene nanoplatelets (GNPs)-reinforced polymer matrix composites for automotive applications.

2. Strategy formulation and analytical framework

2.1. Fundamentals of kinematics and micromechanical analysis

2.1.1. Local constitutive equations

Let us consider a micro-heterogeneous and macro-homogeneous material of volume V subjected to a thermomechanical loading defined by stress and temperature state. Thus, at a point r of the material at the local scale, different physical mechanisms contribute to the total strain $\boldsymbol{\varepsilon}(r)$ yielding:

$$\boldsymbol{\varepsilon}(r) = \boldsymbol{\varepsilon}^e(r) + \boldsymbol{\varepsilon}^\theta(r) + \boldsymbol{\varepsilon}^p(r) \tag{1}$$

where $\boldsymbol{\varepsilon}^e(r)$ represents the elastic strain, while $\boldsymbol{\varepsilon}^\theta(r)$ states for the thermal strain and $\boldsymbol{\varepsilon}^p(r)$ denoting the inelastic strain that can be related to plastic deformation, diffusion phenomena, phase transformation etc. The expressions of these strain fields are given such as:

$$\begin{aligned} &\boldsymbol{\varepsilon}^e(r) = \boldsymbol{s}^e(r) : \boldsymbol{\sigma}(r)\ , \\ &\boldsymbol{\varepsilon}^\theta(r) = \boldsymbol{\alpha}(r)\Delta\theta\ , \\ &\boldsymbol{\varepsilon}^p(r) = \boldsymbol{s}^p(r) : \boldsymbol{\sigma}(r) \end{aligned} \tag{2}$$

with $\boldsymbol{s}^e(r)$ representing the elastic compliance, $\boldsymbol{\alpha}(r)$ denoting the thermal expansion tensor, whereas $\Delta\theta$ is the change in temperature with respect to a reference temperature θ and corresponding rate $\Delta\dot{\theta}$ assumed to be homogeneous for the considered material volume. In Eq. (2), $\boldsymbol{s}^p$ states for the tangent plastic compliance tensor and $\boldsymbol{\sigma}(r)$ is the local stress field. By accounting for the strain tensors in Eq. (2), the local constitutive equation can be written like:

$$\boldsymbol{\varepsilon}(r) = \boldsymbol{s}(r) : \boldsymbol{\sigma}(r) + \boldsymbol{\alpha}(r)\Delta\theta \tag{3}$$

where $\boldsymbol{s}(r) = \boldsymbol{s}^e(r) + \boldsymbol{s}^p(r)$. The global thermomechanical constitutive behaviour of the micro-heterogeneous and macro-homogeneous linking the macro strain $\boldsymbol{E}$ to the macro stress $\boldsymbol{\Sigma}$ through the increment of temperature $\Delta\theta$ takes the form:

$$\begin{aligned} &\boldsymbol{E} = \boldsymbol{S}^{\text{eff}} : \boldsymbol{\Sigma} + \boldsymbol{\alpha}^{\text{eff}}\ \Delta\theta\ , \quad or \\ &E_{ij} = S^{\text{eff}}_{ijkl}\ \Sigma_{kl} + \alpha^{\text{eff}}_{ij}\ \Delta\theta \end{aligned} \tag{4}$$

In Eq. (4), the macro strain $\boldsymbol{E}$ and the macro stress $\boldsymbol{\Sigma}$ are obtained using the average equation $(\cdot)^{eff} = \overline{(\cdot)} = \frac{1}{V}\int_V (\cdot) dV$ over the local strain $\boldsymbol{\varepsilon}(r)$ and local stress $\boldsymbol{\sigma}(r)$ such as:

$$\boldsymbol{E} = \overline{\boldsymbol{\varepsilon}(r)} = \frac{1}{V}\int_V \boldsymbol{\varepsilon}(r)dV \ , \qquad \boldsymbol{\Sigma} = \overline{\boldsymbol{\sigma}(r)} = \frac{1}{V}\int_V \boldsymbol{\sigma}(r)dV \tag{5}$$

The dual form of the Eq. (3) takes the following form:

$$\boldsymbol{\sigma}(r) = \boldsymbol{c}(r) : \boldsymbol{\varepsilon}(r) - \boldsymbol{\beta}(r)\Delta\theta \tag{6}$$

with $\boldsymbol{c}(r)$ denoting the stiffness tensor embedding the inelastic behaviour of the material and thermal stress tensor $\boldsymbol{\beta}(r)$ stating for the:

$$\boldsymbol{c}(r) = \boldsymbol{s}^{-1}(r) \ , \quad or \quad c_{ijkl}(r) = s^{-1}_{ijkl}(r) \qquad \boldsymbol{\beta}(r) = \boldsymbol{c}(r) : \boldsymbol{\alpha}(r) \ , \quad or \quad \beta_{ij}(r) = c_{ijkl}(r)\alpha_{kl}(r) \tag{7}$$

Thus,

$$\boldsymbol{\Sigma} = \boldsymbol{C}^{eff} : \boldsymbol{E} - \boldsymbol{\beta}^{eff}\Delta\theta \ , \quad or \quad \Sigma_{ij} = C^{eff}_{ijkl}E_{kl} - \beta^{eff}_{ij}\Delta\theta \tag{8}$$

where,

$$\boldsymbol{C}^{eff} = \left[\boldsymbol{S}^{eff}\right]^{-1} \ , \quad or \quad C^{eff}_{ijkl} = \left[S^{eff}\right]^{-1}_{ijkl} \qquad \boldsymbol{\beta}^{eff} = \boldsymbol{C}^{eff} : \boldsymbol{\alpha}^{eff} \ , \quad or \quad \beta^{eff}_{ij} = C^{eff}_{ijkl}\alpha^{eff}_{kl} \tag{9}$$

2.1.2. Local and global concentration tensors

For a homogeneous medium, the decomposition of local tensors $\boldsymbol{c}(r)$ and $\boldsymbol{\beta}(r)$ can be split into uniform $\boldsymbol{c}^R$ and $\boldsymbol{\beta}^R$ and fluctuation $\delta\boldsymbol{c}$ and $\delta\boldsymbol{\beta}$ parts following the expressions below:

$$c_{ijkl}(r) = c^R_{ijkl} + \delta c_{ijkl}(r), \quad \beta_{ij}(r) = \beta^R_{ij} + \delta\beta_{ij}(r) \tag{10}$$

Considering that the inhomogeneous microstructure would satisfy behavioural relation of Eq. (6) along with the deformation's compatibility equation:

$$\varepsilon_{ij}(r) = \frac{1}{2}\left[u_{i,j}(r) + u_{j,i}(r)\right] = u_{i,j}(r) \tag{11}$$

and the equilibrium equation:

$$\sigma_{ij,j}(r) = 0 \tag{12}$$

Equations (10), (11) and (12) could be written in the form:

$$c^R_{ijkl}u_{k,lj}(r) + \left[\delta c_{ijkl}(r)u_{k,l} - \delta\beta_{ij}(r)\Delta\theta\right]_{,j} = 0 \tag{13}$$

The classic concept of Green's function [52,53] is one of the most powerful means for solving boundary value problems in linear elasticity based on the superposition principle (i.e. the sum of solutions to a given problem is a solution). The nonlinear constitutive behaviour of composites with a periodic microstructure can also be treated with a Green's function approach as shown in the expositions by Eshelby [54] Korringa [55], Zeller and Dederichs [56]. Using the Green tensor technique, Eq. (13) may be transformed into an integral equation (Green's displacement function, see Appendix A):

$$u_m(r) = U^R_m + \int_V G_{mi}(r-r')\left[\delta c_{ijkl}(r')u_{k,l}(r') - \delta\beta_{ij}(r')\Delta\theta\right]_{,j}dV' \tag{14}$$

or

$$u_{m,n}(r) = U^R_{m,n} + \int_V G_{mi,n}(r-r')\left[\delta c_{ijkl}(r')u_{k,l}(r') - \delta\beta_{ij}(r')\Delta\theta\right]_{,j}dV' \tag{15}$$

Thus using Eqs. (11) and (15):

$$\varepsilon_{mn}(r) = E^R_{mn} - \int_V \Gamma_{mnij}(r-r')\left[\delta c_{ijkl}(r')\varepsilon_{kl}(r') - \delta\beta_{ij}(r')\Delta\theta\right]dV' \tag{16}$$

where $\boldsymbol{E}^R$ is the total strain of the reference homogeneous medium subjected to the same boundary conditions as the effective medium:

$$E^R_{mn} = \frac{1}{2}\left(U^R_{m,n} + U^R_{n,m}\right) \ , \qquad \Gamma_{mnij}(r-r') = -\frac{1}{2}\left[G_{mi,jn}(r-r') + G_{ni,jm}(r-r')\right] \tag{17}$$

Under the assumption of Eshelby inclusion [54] and assuming that $\boldsymbol{c}^R$ and $\boldsymbol{\beta}^R$ are piecewise constant, we can write:

$$\begin{cases} \delta c(r) = \sum_{I=0}^{N}\left(\boldsymbol{c}^I - \boldsymbol{c}^R\right)\aleph^I(r) = \sum_{I=0}^{N}\Delta\boldsymbol{c}^I\aleph^I(r) \\ \delta\beta(r) = \sum_{I=0}^{N}\left(\boldsymbol{\beta}^I - \boldsymbol{\beta}^R\right)\aleph^I(r) = \sum_{I=0}^{N}\Delta\boldsymbol{\beta}^I\aleph^I(r) \end{cases} \tag{18}$$

where $\Delta\boldsymbol{c} = \boldsymbol{c}^I - \boldsymbol{c}^R, \Delta\boldsymbol{\beta} = \boldsymbol{\beta}^I - \boldsymbol{\beta}^R$ and indicator function $\aleph^I(r) = \begin{cases} 1 & \forall r \in V^I \\ 0 & \forall r \notin V^I \end{cases}$ associated with the phase I constituent.

The average strain $\boldsymbol{\varepsilon}^I$ inside material of phase I can therefore be calculated:

$$\boldsymbol{\varepsilon}^I = \frac{1}{V^I}\int_{V^I}\boldsymbol{\varepsilon}(r)dV \tag{19}$$

Thus from Eq. (16) in (19):

$$\boldsymbol{\varepsilon}^I = \boldsymbol{E}^R - \frac{1}{V^I}\sum_{J=1}^{N}\left[\iint_{V^IV^J}\Gamma(r-r') : \left[\Delta c^J : \boldsymbol{\varepsilon}^J - \Delta\boldsymbol{\beta}^J\Delta\theta\right]dVdV'\right] \tag{20}$$

Leading to presenting the unknown total strain of each constituent as (see Appendix A):

$$\begin{cases} \boldsymbol{\varepsilon}^I = \boldsymbol{E}^R - \sum_{J=1}^{N}\boldsymbol{T}^{IJ} : \left[\Delta\boldsymbol{c}^J : \boldsymbol{\varepsilon}^J - \Delta\boldsymbol{\beta}^J\Delta\theta\right] \\ I = 0, 1, 2, \cdots\cdots, N \end{cases} \tag{21}$$

where,

$$\boldsymbol{T}^{II} = \frac{1}{V^I}\int_{V^I}\int_{V^I}\Gamma(r-r')dVdV' \ , \qquad \boldsymbol{T}^{IJ} = \frac{1}{V^I}\int_{V^I}\int_{V^J}\Gamma(r-r')dVdV' \tag{22}$$

The solution of Eq. (21) can be written in the form of localisation expression relating to the strain of reference medium $\boldsymbol{E}^R$ and the temperature increment $\Delta\theta$ as:

$$\boldsymbol{\varepsilon}^I = \boldsymbol{R}^I : \boldsymbol{E}^R + \boldsymbol{r}^I\Delta\theta \tag{23}$$

where $\boldsymbol{R}^I$ and $\boldsymbol{r}^I$ are concentration tensors of the inclusion for dilute or local mechanical and thermal strain localisation or, respectively, relative to the reference medium. Substituting Eq. (23) into Eq.(21) and solving for $\boldsymbol{R}^I$ and $\boldsymbol{r}^I$ yields:

$$\begin{cases} \left(\boldsymbol{R}^I\right)_{i+1} = \left(\mathbf{I} + \boldsymbol{T}^{II} : \Delta\boldsymbol{c}^I\right)^{-1} : \left(\mathbf{I} - \sum_{\substack{J=0 \\ J\neq I}}^{N}\boldsymbol{T}^{IJ} : \Delta\boldsymbol{c}^J : \left(\boldsymbol{R}^J\right)_i\right) \\ \left(\boldsymbol{r}^I\right)_{i+1} = \left(\mathbf{I} + \boldsymbol{T}^{II} : \Delta\boldsymbol{c}^I\right)^{-1} : \left(\boldsymbol{T}^{II} : \Delta\boldsymbol{\beta}^I + \mathbf{I} - \sum_{\substack{J=0 \\ J\neq I}}^{N}\boldsymbol{T}^{IJ} : \left[\Delta\boldsymbol{\beta}^J - \Delta\boldsymbol{c}^J : \left(\boldsymbol{r}^J\right)_i\right]\right) \\ I = 0, 1, 2, 3, \cdots., N \end{cases} \tag{24}$$

Expression in Eq. (24) are written in their implicit form to be solved iteratively, where subscripts (i) et $(i+1)$ are the iteration step numbers, $\mathbf{I}$ is the fourth-order symmetric identity tensor $\mathrm{I}_{ijkl} = \frac{1}{2}\left(\delta_{ik}\delta_{jl} + \delta_{il}\delta_{jk}\right)$, whereas $N+1$ denotes the number of phases considered in a composite material (matrix phase (o)). To start this iterative process, initial approximation values of $\boldsymbol{R}^I_{(0)} = \left(\mathbf{I} + \boldsymbol{T}^{II} : \left(\boldsymbol{c}^I - \boldsymbol{c}^R\right)\right)^{-1}$ and $\boldsymbol{r}^I_{(0)} = \boldsymbol{R}^I_{(0)} : \boldsymbol{T}^{II} : \Delta\boldsymbol{\beta}^I$ leading to converging, are obtained by neglecting the influence of all constituents on relative concentration tensors of I th element [57,58]. $\boldsymbol{T}^{II}$ and $\boldsymbol{T}^{IJ}$ are the interaction tensors for One-site (OS) and Multi-site (MS)

modelling, respectively. General expressions for $\boldsymbol{T}^{II}$ and $\boldsymbol{T}^{IJ}$ as well as their numerical implementation are provided in Appendix A. The global fourth-order mechanical $\boldsymbol{A}^I$ and second-order thermal $\boldsymbol{a}^I$ strain concentration tensors can next be deduced from tensors $\boldsymbol{R}^I$ and $\boldsymbol{r}^I$. Volume averaging of Eq. (23) leads to the following relations:

$$\begin{cases} \overline{\boldsymbol{\varepsilon}^I} = \overline{\boldsymbol{R}^I} : \boldsymbol{E}^R + \overline{\boldsymbol{r}^I}\Delta\theta = E \\ \boldsymbol{E}^R = \left(\overline{\boldsymbol{R}^I}\right)^{-1} : \left(\boldsymbol{E} - \overline{\boldsymbol{r}^I}\Delta\theta\right) \end{cases} \tag{25}$$

Substituting Eq.(25) into Eq. (23):

$$\boldsymbol{\varepsilon}^I = \left[\boldsymbol{R}^I : \left(\overline{\boldsymbol{R}^I}\right)^{-1}\right] : \boldsymbol{E} + \left[\boldsymbol{r}^I - \boldsymbol{R}^I : \left(\overline{\boldsymbol{R}^I}\right)^{-1} : \overline{\boldsymbol{r}^I}\right]\Delta\theta \tag{26}$$

Global localisation tensors, therefore:

$$\begin{cases} \boldsymbol{A}^I = \boldsymbol{R}^I : \left(\overline{\boldsymbol{R}^I}\right)^{-1} \\ \boldsymbol{a}^I = \boldsymbol{r}^I - \boldsymbol{R}^I : \left(\overline{\boldsymbol{R}^I}\right)^{-1} : \overline{\boldsymbol{r}^I} \end{cases} \tag{27}$$

2.2. Mori-Tanaka (MT) scheme formulation

Mori–Tanaka (MT) formulation [59] is a homogenisation model built on the concept of Eshelby's dilute model [54]. The MT scheme considers the matrix phase-(o) in a composite material to be the reference medium ($\boldsymbol{c}^o = \boldsymbol{c}^R$) and the average strain field inside the matrix is approximated by the strain within the reference medium ($\varepsilon^o \cong \boldsymbol{E}^R$). The MT scheme allows us to introduce kinematic equation without the unknown tensors $\boldsymbol{T}^{oo}$ and $\boldsymbol{T}^{Io}$. This leads to $\varepsilon^o \cong \boldsymbol{E}^o$, with $\boldsymbol{E}^o$ being the local strain of the considered volume V having the matrix properties, thus, $\boldsymbol{R}^0 = \mathbf{I}$, $\boldsymbol{r}^0 = 0$. Therefore, one gets:

$$\begin{cases} \boldsymbol{A}^0 = \boldsymbol{R}^0 : \left(\overline{\boldsymbol{R}^I}\right)^{-1} = \left[\mathbf{I} - \sum_{I=1}^{N} f_I\left(\mathbf{I} - \boldsymbol{R}^I\right)\right]^{-1} \\ \boldsymbol{a}^0 = \boldsymbol{r}^0 - \boldsymbol{A}^0 : \overline{\boldsymbol{r}^I} = -\boldsymbol{A}^0 : \sum_{I=1}^{N} f_I \boldsymbol{r}^I \\ \boldsymbol{A}^I = \boldsymbol{R}^I : \left(\overline{\boldsymbol{R}^I}\right)^{-1} = \boldsymbol{R}^I : \boldsymbol{A}^0 \\ \boldsymbol{a}^I = \boldsymbol{r}^I - \boldsymbol{A}^I : \overline{\boldsymbol{r}^I} = \boldsymbol{r}^I + \boldsymbol{R}^I : \boldsymbol{a}^0 \end{cases} \tag{28}$$

where, f_I is volume fraction. Finally, the effective properties of a heterogeneous or composite material are then deduced from the following relations:

$$\begin{cases} \boldsymbol{C}^{eff} = \boldsymbol{c}^0 + \sum_{I=1}^{N} f_I\left(\boldsymbol{c}^I - \boldsymbol{c}^0\right) : \boldsymbol{A}^I \\ \boldsymbol{\beta}^{\text{eff}} = \boldsymbol{\beta}^0 + \sum_{I=1}^{N} f_I\left[\left(\boldsymbol{\beta}^I - \boldsymbol{\beta}^0\right) - \left(\boldsymbol{c}^I - \boldsymbol{c}^0\right) : \boldsymbol{a}^I\right] \\ \boldsymbol{\Sigma} = \boldsymbol{C}^{\text{eff}} : \boldsymbol{E} - \boldsymbol{\beta}^{\text{eff}}\Delta\theta \end{cases} \tag{29}$$

2.3. Rate dependent behaviour

2.3.1. Viscoplastic response (VP)

Miled et al. [60] used the classic J_2 plasticity model with isotropic hardening to represent the viscoplastic effects of a composite material. As a result, the plastic flow criterion based on the J_2 theory is given by:

$$\begin{cases} f\left(\sigma_{eq}, p, \dot{\varepsilon}\right) = \sigma_{eq} - \left[\sigma_y(\dot{\varepsilon}) + R(p)\right] \\ \sigma_{eq} = \sqrt{\frac{3}{2}\mathbf{s} : \mathbf{s}} \end{cases} \tag{30}$$

Where σ_{eq} is the equivalent stress of von Mises, σ_y is the yield stress indicating the elasticity limit (which may depend on the strain rate deformation) and $R(p)$ is the hardening function. The accumulative plastic deformation p is an internal variable that preserves the history of viscoplastic deformation. It is given such as:

$$\begin{cases} p(t) = \int_0^t \dot{p}(\tau)d\tau \\ \dot{p} = \sqrt{\frac{2}{3}\dot{\boldsymbol{\varepsilon}}^{vp} : \dot{\boldsymbol{\varepsilon}}^{vp}} \end{cases} \tag{31}$$

The viscoplastic strain rate follows a plastic flow rule:

$$\dot{\boldsymbol{\varepsilon}}^{vp} = \dot{p}\frac{\partial f}{\partial \boldsymbol{\sigma}} = \dot{p}\boldsymbol{N} \tag{32}$$

where the tensor $\boldsymbol{N}$ is given by:

$$\begin{cases} \boldsymbol{N} = \frac{3}{2}\frac{\mathbf{s}}{\sigma_{eq}} \\ \boldsymbol{N} : \boldsymbol{N} = \frac{3}{2} \end{cases} \tag{33}$$

and the viscoplastic multiplier $\dot{p}$ is defined by a viscoplastic function g_v such as:

$$\begin{cases} \dot{p} = 0 & \text{if } f \le 0 \\ \dot{p} = g_v\left(\sigma_{eq}, p, \dot{\varepsilon}\right) & \text{if } f > 0 \end{cases} \tag{34}$$

2.3.2. Computing algorithm

Considering finite stress and strain increments, an algorithmic tangent operator can $\boldsymbol{C}^{\text{alg}}$ be derived from a coherent linearization of the constitutive equations that are integrated over time t_{n+1} around the solution such as:

$$\delta\boldsymbol{\sigma}(t_{n+1}) = \boldsymbol{C}^{\text{alg}} : \delta\boldsymbol{\varepsilon}(t_{n+1}) \tag{35}$$

where δ means a total variation at t_{n+1} The use of a radial return mapping algorithm in elasto-viscoplastics allows the algorithmic tangent operator to be obtained by [50]:

$$\begin{cases} \boldsymbol{C}^{\text{alg}} = \boldsymbol{C}^{el} - \frac{(2G)^2}{h_v}\boldsymbol{N}\otimes\boldsymbol{N} - (2G)^2\frac{\sigma_{eq}\Delta p}{\sigma_{eq}+3G\Delta p}\frac{\partial \boldsymbol{N}}{\partial \boldsymbol{\sigma}} - \frac{2G}{h_v g_{,\sigma}}\boldsymbol{N}\otimes g_{,\varepsilon} \\ h_v = \frac{1}{(\Delta t)g_{,\sigma}} + 3G - \frac{g_{,p}}{g_{,\sigma}} \\ g_{,\sigma} = \frac{\partial g_v}{\partial \sigma_{eq}};\ g_{,p} = \frac{\partial g_v}{\partial p};\ g_{,\varepsilon} = \frac{1}{\Delta t}\frac{\partial g_v}{\partial \dot{\varepsilon}} \end{cases} \tag{36}$$

When the elasticity limit σ_y is constant, then $g_{,\varepsilon} = 0$ and the algorithmic tangent operator becomes symmetric as an expression identical to that obtained in Doghri [61]. The expressions of σ_y and $g_{,p}$ depend on the viscoplastic (VP) function g_v that would be taken under consideration, e.g. Norton's law [62]. Odqvist [63,64] generalized the classical uniaxial stress Norton's law of $\dot{\varepsilon} = A\sigma^m$ where A and m are material constants. In the general multiaxial stress state Norton's power law (initial yield Norton law) would be [65]:

$$g_{v\left(\sigma_{eq},p\right)} = \begin{cases} \frac{\sigma_y}{\eta}\left(\frac{f}{\sigma_y}\right)^m & \text{if } f > 0 \\ 0 & \text{else} \end{cases} \tag{37}$$

where η [Pa s] and m are the viscoplastic modulus and the exponent, respectively. One can calculate:

$$\begin{aligned} g_{,\sigma} &= \frac{m}{\eta}\left(\frac{f}{\sigma_y}\right)^{m-1}, \\ \frac{g_{,p}}{g_{,\sigma}} &= -\frac{dR}{dp}, \\ h_v &= \frac{\eta}{m(\Delta t)}\left(\frac{f}{\sigma_y}\right)^{1-m} + 3G + \frac{dR}{dp} \end{aligned} \tag{38}$$

The notion of excessive stress can also be accounted for by using another VP power law function (current yield Norton law) [66] according to Perzyna's approach [67,68,69] with two parameters: the

viscoplastic modulus ($\kappa[1/s]$) and the exponent (m) that appear as follows:

$$g_{v(\sigma_{eq},p)} = \begin{cases} \kappa\left(\dfrac{f}{\sigma_y + R(p)}\right)^m & if \quad f > 0 \\ 0 & else \end{cases} \tag{39}$$

In this case:

$$\begin{cases} g_{,\sigma} = m\dfrac{g_v}{f} \\ g_{,p} = -mg_v\dfrac{dR}{dp}\left(\dfrac{1}{f} + \dfrac{1}{\sigma_y + R(p)}\right) \\ h_v = \dfrac{f}{mg_v(\Delta t)} + 3G + \dfrac{dR}{dp}\dfrac{\sigma_{eq}}{\sigma_y + R(p)} \end{cases} \tag{40}$$

In Eq. (37), the initial yield stress σ_y is considered constant. However, in Eq. (39) version of Norton law, the yield stress σ_y and the hardening stress $R(p)$ are considered, i.e. the viscoplastic stress is being updated as the hardening stress increases resulting in more accurate results than the first one, and hence it is utilised in our model.

From the algorithmic tangent operator $\boldsymbol{C}^{alg}$ given by Eq. (36) and using the hypothesis $g_{,\varepsilon} = 0$, one gets:

$$\begin{cases} \boldsymbol{C}^{alg} = \boldsymbol{C}^{el} - \dfrac{(2G)^2}{h_v}\boldsymbol{N}\otimes\boldsymbol{N} - (2G)^2\dfrac{\sigma_{eq}\Delta p}{\sigma_{eq} + 3G\Delta p}\dfrac{\partial \boldsymbol{N}}{\partial \sigma} \\ \boldsymbol{C}^{el} = 2G\mathbf{I}^{dev} + 3K\mathbf{I}^{vol} \\ h_v = \dfrac{1}{(\Delta t)g_{,\sigma}} + 3G - \dfrac{g_{,p}}{g_{,\sigma}} \end{cases} \tag{41}$$

2.3.3. Regulation of the algorithmic tangent operator

From Eq. (36) it can be shown that $h_v \to \infty$ for very small increments of time i.e. when $\Delta t \to 0$, a fact which is unacceptable (because $\boldsymbol{C}^{alg}$ then approaches $\boldsymbol{C}^{el}$ although $\dot{\varepsilon}^{vp} \neq 0$). To solve the problem, Doghri et al. [70] have developed a method of regulation in elasto-viscoplastic from a 1D analytical tangent expression valid for the simplest case (uniaxial-monotonous tension, constant deformation velocity, linear isotropic hardening and linear viscous stress).

$$\begin{cases} \boldsymbol{C}^{reg}(t_{n+1}) = \boldsymbol{C}^{\mathrm{cp}}(t_{n+1}) + [\boldsymbol{C}^{reg}(t_n) - \boldsymbol{C}^{\mathrm{cp}}(t_{n+1})]exp\left(-\dfrac{h_{\mathrm{ep}}}{h_v - h_{\mathrm{ep}}}\right) \\ \boldsymbol{C}^{\mathrm{cp}} = \boldsymbol{C}^{el} - \dfrac{(2G)^2}{h_{\mathrm{ep}}}\boldsymbol{N}\otimes\boldsymbol{N} \\ h_{\mathrm{ep}} = 3G - \dfrac{g_{,p}}{g_{,\sigma}} \end{cases} \tag{42}$$

The algorithmic tangent operator obtained from the Eq. (42) will serve as properties of the nonlinear phase in the homogenisation process obtained by Eq. (29). From this model, validations and numerical applications will be carried out on data from the literature and composites with particles and fibres.

3. Algorithms for solving the effective properties

3.1. Analytical procedure

Considering the 3-phases hierarchical graphene-reinforced polymer nanocomposite (HGPNC), the total volume fraction is given such as $\phi = \phi_F + \phi_G + \phi_o = 1$, where ϕ_F, ϕ_G, ϕ_o represent the volume fraction of the fibres, the GNPs, and the polymer matrix, respectively. As within the 2-phases graphene-based polymer nanocomposite (GPNC), the volume fractions of GNP and the polymer matrix are,

$$\mathrm{v}_G = \frac{\phi_G}{\phi_G + \phi_o}, \quad \mathrm{v}_o = \frac{\phi_o}{\phi_G + \phi_o} = 1 - \mathrm{v}_G \tag{43}$$

respectively. If the manufacturing or design process requires v_G and v_o to be determined first as 2-phase composite then afterwards a third phase of ϕ_F is to be added, the volume fractions would be calculated as,

$$\phi_G = \mathrm{v}_G(1 - \phi_F) \tag{44}$$

with the required value of ϕ_F, ϕ_G is calculated and, $\phi_o = 1 - \phi_G - \phi_F$. The algorithm starts with the strain increment $\boldsymbol{\Delta\varepsilon}$, time step, temperature increment and thermal expansion coefficient (CTE) as the input. $\boldsymbol{\Delta\varepsilon}$ is then split between the phases of the 3-phases HGPNC composite. Considering multiscale modelling with two- sequential levels, at the first level, Voigt assumption $(\mathbf{A}_F^{Old} = \mathbf{I})$ states the strain increment in the fibres while strain averaging represents the strain increment in the 2-phases GPNC composite considered as a matrix. Within the 2-phases GPNC composite, the strain increment is once more divided between the graphene inclusions and the polymer matrix. After a convergence check, the modified Mori–Tanaka scheme for imperfect interfaces computes the effective properties of the 2-phases GPNC composite. At the second level, the effective properties for the 2-phases GPNC composite are used conjunctly with the algorithmic tangent modulus of the fibres to provide the whole 3-phases HGPNC composite with effective tangent modului through a convergence checking. Considering a time interval $[t_n, t_{n+1}]$, strain increment $\boldsymbol{\Delta\varepsilon}$ and thermal instantaneous $\Delta\boldsymbol{\varepsilon}^{\theta}$ such as $\boldsymbol{\varepsilon}_{\mathbf{n+1}} = \boldsymbol{\varepsilon}_{\mathbf{n}} + \boldsymbol{\Delta\varepsilon} + \Delta\boldsymbol{\varepsilon}^{\theta}$ input for the algorithm. The below steps summarise numerical implementation of the incremental algorithm in Fig. 1.

i. Initialization of the strain increment in the fibre phase $\boldsymbol{\Delta\varepsilon}^F \leftarrow \boldsymbol{\Delta\varepsilon} + \Delta\boldsymbol{\varepsilon}^{\theta}$, where $\boldsymbol{\Delta\varepsilon}^F = \mathbf{A}_F : \Delta\varepsilon$ such as $\mathbf{A}_F = \mathbf{I}$.
ii. Update the stress and compute the algorithmic moduli $\boldsymbol{C}_F^{reg}$ in fibre phase using Eqs. (42).
iii. Apply the mid-point rule at time $t_{n+\alpha}$ to the algorithmic moduli of the fibres $\boldsymbol{C}_F^{reg}$ using $\boldsymbol{C}_{r_{(n+\alpha)}}^{reg} = (1-\boldsymbol{\alpha}_x)\boldsymbol{C}_{r_n}^{reg} + \boldsymbol{\alpha}_x\boldsymbol{C}_{r_{n+1}}^{reg}$, $\boldsymbol{r} = \boldsymbol{F}; \boldsymbol{\alpha}_x \in [0,1]$
iv. Compute the average strain increment in the 2-phases GPNC composite phase $\boldsymbol{\Delta}\varepsilon^{Go} = \frac{\boldsymbol{\Delta\varepsilon} - \phi_F\boldsymbol{\Delta}\varepsilon^F}{1-\phi_F}$
v. Initialization of the strain increment in the graphene phase $\boldsymbol{\Delta}\varepsilon^G \leftarrow \boldsymbol{\Delta}\varepsilon^{Go}$, where $\boldsymbol{\Delta}\varepsilon^G = \mathbf{A}_G : \boldsymbol{\Delta}\varepsilon^{Go}$ such as $\mathbf{A}_G = \mathbf{I}$.
vi. Update the stress and compute the algorithmic moduli $\boldsymbol{C}_G^{reg}$ in graphene phase using Eqs. (42).
vii. Apply the mid-point rule at time $t_{n+\alpha}$ to the algorithmic moduli of the graphene $\boldsymbol{C}_G^{reg}$ using $\boldsymbol{C}_{r_{(n+\alpha)}}^{reg} = (1-\boldsymbol{\alpha}_x)\boldsymbol{C}_{r_n}^{reg} + \boldsymbol{\alpha}_x\boldsymbol{C}_{r_{n+1}}^{reg}$, $\boldsymbol{r} = \boldsymbol{G}; \boldsymbol{\alpha}_x \in [0,1]$
viii. Initialization of the strain increment in the polymer matrix $\boldsymbol{\Delta}\varepsilon^o \leftarrow \boldsymbol{\Delta}\varepsilon^{Go}$, where $\boldsymbol{\Delta}\varepsilon^G = \frac{\boldsymbol{\Delta}\varepsilon^{Go} - \mathrm{v}_G\boldsymbol{\Delta}\varepsilon^G}{1-\mathrm{v}_G}$ such as $\mathbf{A}_o = \mathbf{I}$.
ix. Update the stress and compute the algorithmic moduli $\boldsymbol{C}_o^{reg}$ in polymer matrix using Eqs. (42).
x. Apply the mid-point rule at time $t_{n+\alpha}$ to the algorithmic moduli of the polymer matrix $\boldsymbol{C}_o^{reg}$ using $\boldsymbol{C}_{r_{(n+\alpha)}}^{reg} = (1-\boldsymbol{\alpha}_x)\boldsymbol{C}_{r_n}^{reg} + \boldsymbol{\alpha}_x\boldsymbol{C}_{r_{n+1}}^{reg}, \boldsymbol{r} = \boldsymbol{o}; \boldsymbol{\alpha}_x \in [0,1]$
xi. Compute the global strain concentration tensors of graphene $\mathbf{A}_G$ and polymer matrix $\mathbf{A}_o$ using Eqs. (28).
xii. Calculate the residual to check the compatibility of average strain in graphene phase $\boldsymbol{R} = \mathbf{A}_G : \boldsymbol{\Delta}\varepsilon^{Go} - \boldsymbol{\Delta}\varepsilon^G$
xiii. If $|\boldsymbol{R}| \leq \mathrm{TOL} = 10^{-8}$, then continue to the next step, else go to step **v** using the computed value of strain concentration tensor $\mathbf{A}_G$
xiv. Compute the effective tangent modulus $\boldsymbol{C}_{Go}^{eff}$ of the 2-phases GPNC composite using Eq. (29).
xv. Apply the mid-point rule at time $t_{n+\alpha}$ to the algorithmic moduli of the 2-phases GPNC composite $\boldsymbol{C}_{Go}^{eff}$ using $\boldsymbol{C}_{r_{(n+\alpha)}}^{reg} = (1-\boldsymbol{\alpha})\boldsymbol{C}_{r_n}^{reg} + \boldsymbol{\alpha}\boldsymbol{C}_{r_{n+1}}^{reg}, \boldsymbol{r} = \boldsymbol{Go}; \boldsymbol{\alpha} \in [0,1]$
xvi. Compute thermal effective tangent modulus $\boldsymbol{\beta}_{Go}^{eff}$ of the 2-phases GPNC composite using Eq. (29).

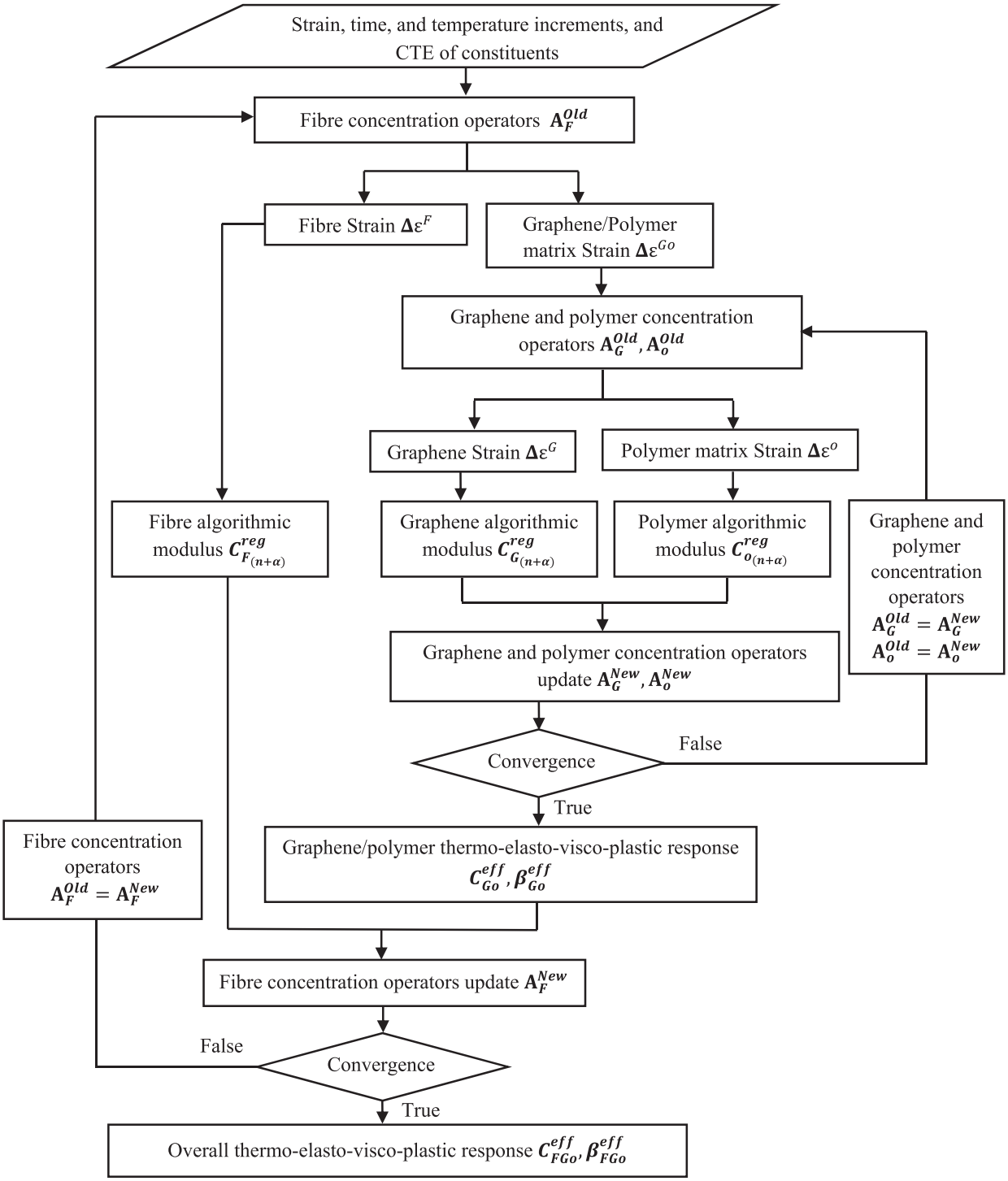

Fig. 1. Algorithm for analytical solution of the 3-phases composite.

xvii. Using $C_{Go_{(n+\alpha)}}^{reg}$ and β_{Go}^{eff} as a matrix phase, compute global strain concentration tensors $\mathbf{A}_F$ of the fibres using Eq. (28).

xviii. Calculate the residual to check the compatibility of average strain in graphene phase $\boldsymbol{R} = \mathbf{A}_F : \Delta\boldsymbol{\varepsilon} - \Delta\varepsilon^F$

xix. If $|\boldsymbol{R}| \leq \text{TOL} = 10^{-8}$, then continue to the next step, else to the step i using the computed value of strain concentration tensor $\mathbf{A}_F$.

xx. Finally, compute the effective tangent modului C_{FGo}^{eff} and β_{FGo}^{eff} of the 3-phases HGPNC composite using Eq. (29).

3.2. Numerical modelling

For the numerical modelling, LS-DYNA finite element (FE) solver [71] is employed as a user-defined material (UMAT). The UMAT is developed in a FORTRAN subroutine using the algorithm shown in Fig. 2. The strain increments $\Delta\boldsymbol{\varepsilon}$ and time steps input for the numerical modelling come from LS-DYNA FE code.

The subroutine reads the material constants, such as the stiffness and strength, from the LS-DYNA input file. Then, using the history variables, material constants, and strain increments, the subroutine follows the same approach as the previous algorithm shown in Fig. 1 to calculate the

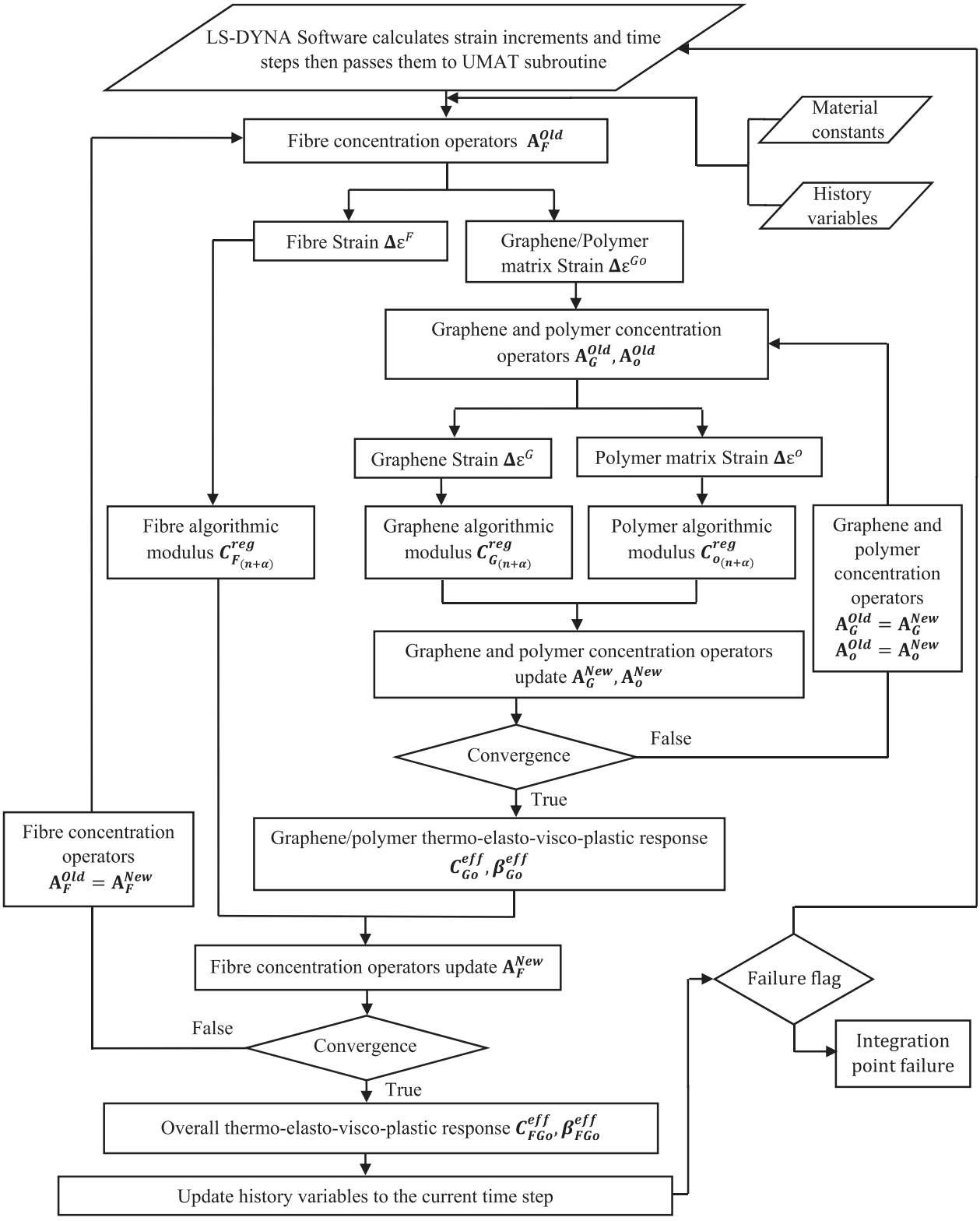

Fig. 2. Algorithm for FE solver of the 3-phases composite nonlinear response.

HGPNC properties at the end of the time step by using the constitutive equations. The subroutine then updates and saves the history variables to the current time step and outputs calculated properties. A flag for failure was set for each integration point; if it were true, the integration point fails; if not, the calculations proceed to the next time step. It should be noted that the failure flag value needs to be as accurate as possible otherwise would result in earlier failure of the integration point.

4. Results and discussions

4.1. Validation

The ability of the present model to reproduce results is examined from the open literature out herein. The model predictions are compared with several earlier works in literature. Li et al. [15] experimented on

carbon nanotubes (CNTs) – Graphene nanoplatelets (GNPs) / epoxy composite. CNTs were considered discontinuous fibres, and GNPs were assumed to be effective rectangular solid fibres. The material properties used for this analysis are presented in Table 1.

Material constants yield strength σ_o, strength coefficient k and strain hardening exponent ɳ were determined based on a comparison between experimental results and theoretical power-law model using Ludwik equation [77]:

$$\sigma = \sigma_0 + k\varepsilon^{\eta} \tag{45}$$

True strains and stresses were converted to their engineering counterparts e and s, respectively, as shown in Fig. 3 using [77]:

$$e = \exp(\varepsilon) - 1\ , \quad s = \sigma/(e+1) \tag{46}$$

Conversion of mass fraction to volume fraction for a 2-phases composite can be calculated using the density of the constituents [74,43,78]. Thus for a 3-phases composite:

$$\begin{aligned}\phi_{CNT} &= \frac{W_{CNT}/\rho_{CNT}}{W_{GNP}/\rho_{GNP} + W_{CNT}/\rho_{CNT} + W_o/\rho_o} \\ &= \frac{W_{CNT}}{W_{CNT} + (\rho_{CNT}/\rho_{GNP})W_{GNP} + (\rho_{CNT}/\rho_o)(1 - W_{GNP} - W_{CNT})}\end{aligned} \tag{47}$$

$$\begin{aligned}\phi_{GNP} &= \frac{W_{GNP}/\rho_{GNP}}{W_{GNP}/\rho_{GNP} + W_{CNT}/\rho_{CNT} + W_o/\rho_o} \\ &= \frac{W_{GNP}}{W_{GNP} + (\rho_{GNP}/\rho_{CNT})W_{CNT} + (\rho_{GNP}/\rho_o)(1 - W_{GNP} - W_{CNT})}\end{aligned} \tag{48}$$

where ϕ_{CNT}, ϕ_{GNP}, W_{CNT} and W_{GNP} are the volume and weight fraction of CNT and GNP, respectively, ϕ_o and W_o are the volume fraction and weight fraction of the matrix, ρ_{CNT} and ρ_{GNP} are the density of CNT and GNP, respectively, and ρ_o is the matrix density. The macro stress–strain response under uniaxial loading is given by a macro strain increment such as $\boldsymbol{\Delta\varepsilon\mu}$ with $\boldsymbol{\mu} = \mathbf{e}_3 \otimes \mathbf{e}_3 - \frac{1}{2}[\mathbf{e}_1 \otimes \mathbf{e}_1 + \mathbf{e}_2 \otimes \mathbf{e}_2]$, where $\mathbf{e}_1 = [1,0,0]$, $\mathbf{e}_2 = [0,1,0]$ and $\mathbf{e}_3 = [0,0,1]$ are unit vectors.

Fig. 4 illustrates the predicted results of the multi-site model versus the experimental work of Li et al. [15]. Considering the total results, Fig. 4(a) combines overall comparisons. Fig. 4(b) specifies epoxy matrix and GNP/epoxy composite, indicating a good trend except that experimental values suffer from ductile damage starting at about 4% strain. Fig. 4(c) indicates no match between the predicted CNT/epoxy composite and the experimental values. This is attributed to the waviness of pristine CNTs, which interfere with predicting the composite behaviour and causes the aspect ratio for CNTs to be meaningless. Thus, the hybrid CNT– GNP reinforced composite, with which the CNTs were grown on GNPs, rendered uniform dispersion and maintained their aspect ratio and shape, resulting in the acceptable prediction of the hybrid CNT–GNP composite behaviour shown in Fig. 4(d). As for the one-site model, results follow the same behaviour predicted for the multi-site model as there is no significant difference between the multi-site and one-site model results for the current composite, as shown in Fig. 5. This outcome was expected because the interactions between reinforcements are negligible due to their small mass fractions within the composite material.

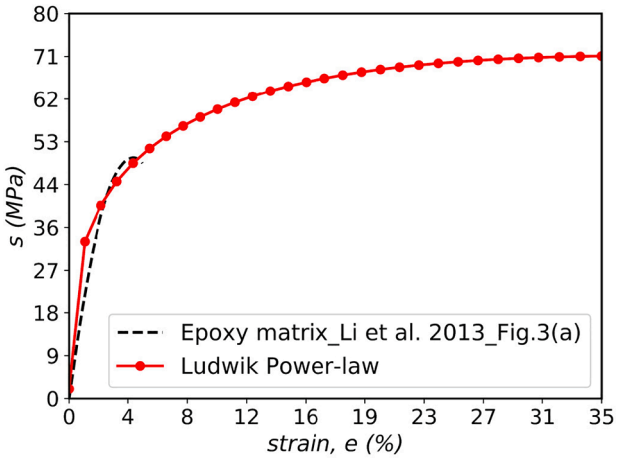

Fig. 3. Experimental values versus power-law flow function.

4.2. Fibre-glass/graphene-reinforced 3-phases composite

4.2.1. Material characteristics

The matrix considered is polyamide PA6-B3K with an isotropic hardening power-law, whereas the graphene nanoplatelets (GNP) and short glass fibres considered elastic are reported in Table 2.

It should be mentioned that the thermal expansion coefficient (CTE) of single-layer graphene has a negative value and is estimated to be −8.0 × 10^{-6} /°C at room temperature [83]. However, graphene CTE is very sensitive to the substrate. A very weak substrate interaction can largely affect the negative CTE value. The CTE will be positive if the substrate interaction is strong enough and the value reaches 20.0 x10^{-6} / °C [82,84].

Fig. 6 compares the one-site model with the multi-site considering the evolution of the effective stress versus the equivalent strain under

Table 1
Material properties of CNT, GNP and epoxy constituents used for validation against Li et al. [15].

Epoxy matrix								
E_o	ν_o	σ_o	k	ɳ	κ [1/s]	m	CTE_o (10^{-6}/K)	ρ_o
2.2[a] GPa	0.3[b]	2 MPa	140 MPa	0.33	150	10	81[c]	1.1[a] g/cm^3
Graphene nanoplatelets (GNPs)								
E_{GNP}	ν_{GNP}	*aspect ratio (AR)*					CTE_{GNP} (10^{-6}/K)	ρ_{GNP}
1000[a,d] GPa	0.22	0.01[e]					7.83[c]	2.25[a] g/cm^3
Carbon nanotubes (CNT)								
E_{CNT}	ν_{CNT}	*aspect ratio (AR)*					CTE_{CNT} (10^{-6}/K)	ρ_{CNT}
450[a,f] GPa	0.22[g]	1000[e]					0.2[h]	1.78[a] g/cm^3

[a] According to Li et al. [15].
[b] According to Chandra et al. [72].
[c] According to Shi et al. [73].
[d] According to Zhao et al. [43].
[e] According to our calculations based on Li et al. [15] inclusion morphology.
[f] According to Rafiee et al. [74].
[g] According to Zeng et al. [75].
[h] According to Deng et al. [76].

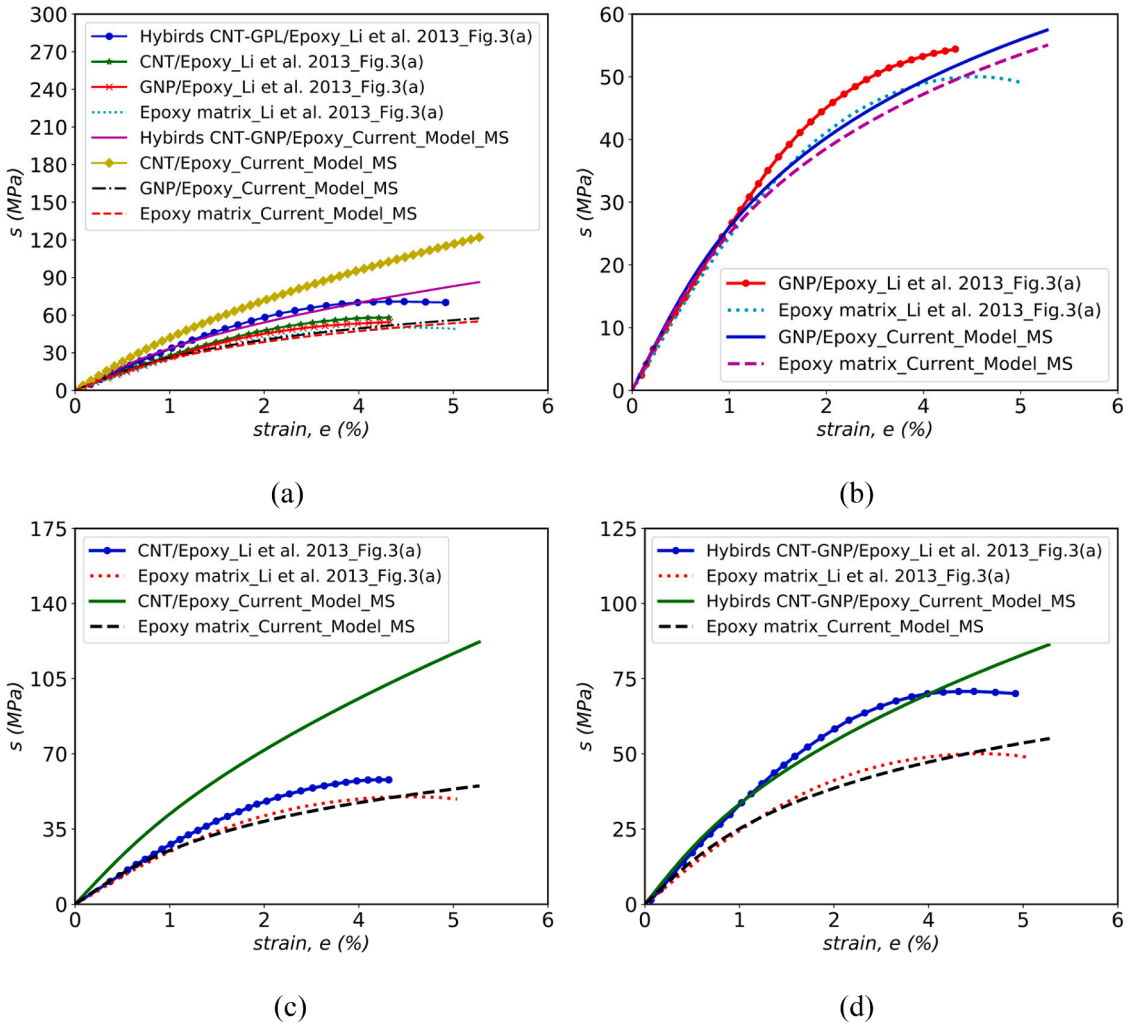

Fig. 4. Tensile stress–strain curves of epoxy matrix and the epoxy composites with 0.5 wt% reinforcements validation for multi-site model at strain rate ($\dot{\varepsilon}$) = 10^{-4} against Li et al. [15]: (a) Combined results (b) GNP composite, (c) CNT composite, and (d) CNT–GNP hybrids with CNTs (0.24 wt%) and GNPs (0.26 wt%).

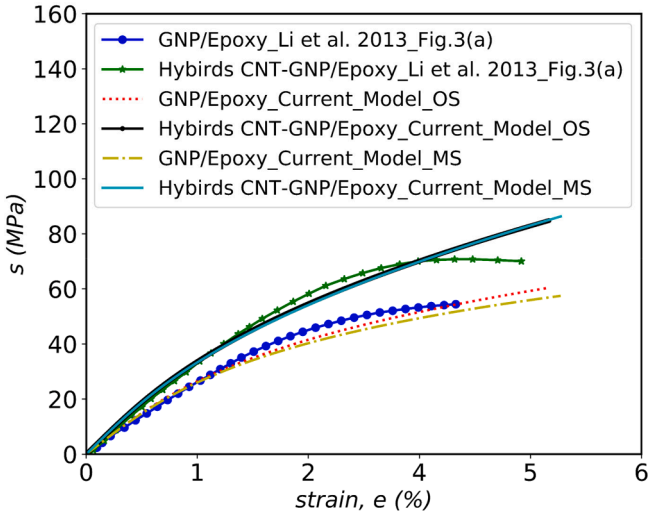

Fig. 5. Tensile stress–strain curves of epoxy matrix and the epoxy composites with 0.5 wt% reinforcements validation for one-site versus multi-site model at strain rate ($\dot{\varepsilon}$) = 10^{-4} against Li et al. [15].

different volume fractions ϕ_F of short glass fibres. The analyses have been conducted for two sets of volume fraction ϕ_F, low and increased volume fractions. As expected, in both cases, the effective behaviour is enhanced with the increase of ϕ_F. The higher the volume fraction ϕ_F, the better the equivalent stress of the 3-phases HGPNC composite material. As seen in Fig. 6, it is apparent that the one-site model exaggerates the enhanced behaviour compared with the multi-site model considering particle interactions. In addition, the higher the volume fraction, the stronger the interactions between reinforcements and the more significant the gap between the two prediction models.

Fig. 7 depicts the effect of graphene on the evolution of the effective stress–strain response of the 3-phases HGPNC composite. As anticipated, results appear to shift towards high stress with increased GNPs volume fraction resulting in increased composite stiffness in terms of Young modulus, initial yield strength and plastic hardening modulus. Fig. 8 indicates the overestimation of the one-site model results against the multi-site model, especially with increasing the volume fraction.

Fig. 9 illustrates the composite behaviour as a function of the strain rate $\dot{\boldsymbol{\varepsilon}}$ and the temperature increment $\Delta\dot{\theta}$ design parameters of one-site model. Fig. 9(a) shows the influence of the strain rate $\dot{\varepsilon}$. This results in a loss of ductility of the composite with increasing $\dot{\varepsilon}$. The influence of the temperature increment $\Delta\dot{\theta}$ has been analyzed in Fig. 9(b). It shows that the more $\Delta\dot{\theta}$ increases, the stress–strain response of the composite slightly deteriorates. The increase in temperature, therefore, exerts a slight decreasing effect on the mechanical performance of the

Table 2
Material properties for E-Glass/G2NAN/PA6-B3K constituent materials [79,80,81].

Polyamide PA6-B3K polymer matrix								
E_o	ν_o	σ_o	k	ɳ	κ [1/s]	m	CTE_o (x10^{-6}/ °C)	ρ_o
2.0 GPa	0.39	60.5 MPa	63 MPa	0.4	150	5	95.0	1.13 g/cm^3
Graphene G2NAN								
E_G	ν_G	*aspect ratio (AR)*					CTE_G (x10^{-6}/ °C)	ρ_G
700 GPa	0.22	10^{-3}					20.0[m,n,p]	2.2 g/cm^3
Short E-Glass fibres								
E_F	ν_F	*aspect ratio (AR)*					CTE_F (x10^{-6}/ °C)	ρ_F
85 GPa	0.23	10					5.0	2.49 g/cm^3

[m] According to Jiang et al. [82].
[n] According to Shi et al. [73].
[p] According to Yoon et al. [83].

composite. Indeed variations in the strain rate $\dot{\varepsilon}$ and temperature $\Delta\dot{\theta}$ have a similar effect on the multi-site model as shown in Fig. 10 however at a less composite stiffness due to the considered interactions of neighbouring inclusions.

4.2.2. Numerical modelling and characterisation

The developed constitutive equations are implemented through a multiscale simulation. Mechanical characterisations based on the ASTM standards are performed on tensile and compression [27]. Tensile specimen geometry recommendations of ASTM-E8M [85] are considered, which are comparable to tensile test specimen dimensions for reinforced composites conforming to the dimensions of the Type I specimen of ASTM D638 [86] and also comparable to ASTM D3039/D3039M [87]. At the same time, compression specimens were based on

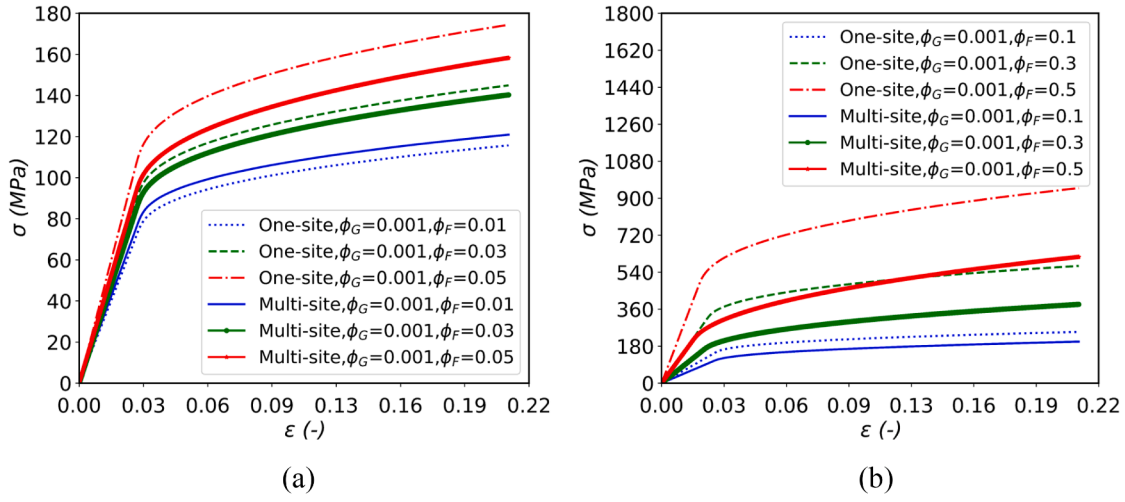

Fig. 6. Comparing one-site model versus multi-site model: (a) low volume fraction, and (b) increasing volume fraction.

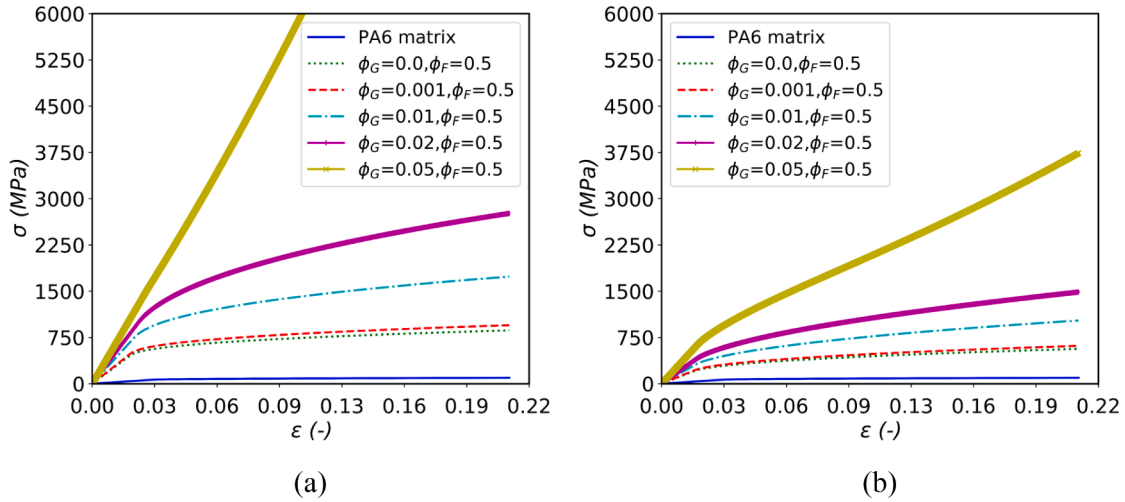

Fig. 7. Effect of graphene constituent on 3-phases E-Glass/G2NAN/PA6-B3K composite under uniaxial loading at strain rate ($\dot{\varepsilon}$) = 10^{-4}: (a) one-site, and (b) multi-site.

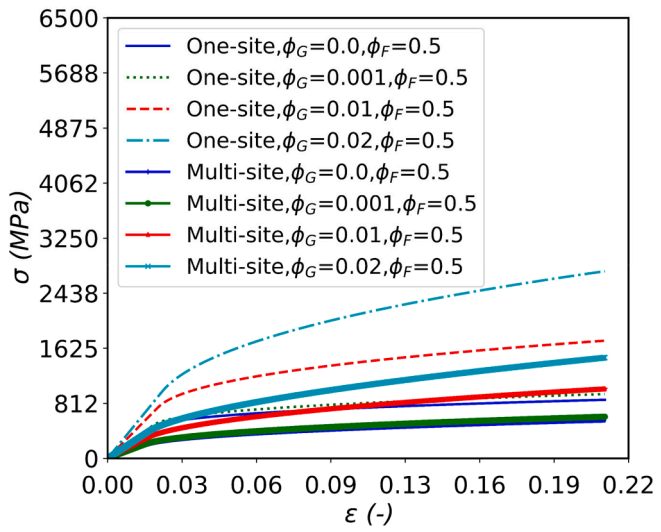

Fig. 8. Comparing one-site versus multi-site considering effect of graphene on 3-phases E-Glass/G2NAN/PA6-B3K composite under uniaxial loading at strain rate ($\dot{\varepsilon}$) = 10^{-4}.

ASTM D695 [88]. Fig. 11 compares analytical and FE tensile testing. Low volume fractions were used to diminish the effect of anisotropy. Overall good agreement is shown between both sets of results using one-site and multi-site models.

Fig. 12 illustrates the development of the effective stress and strain response of the 3-phases HGPNC composite under the tensile test. As obtained previously, the gap between responses is sensitive to the GNP volume fraction. The higher the volume fraction, the higher the gap. The composite stiffness increases as the results shift in the direction of high stress with the increase of the GNP volume fraction. For the compression, similar trends are also observed in terms of increased Young modulus, initial yield strength and plastic hardening modulus, as shown in Fig. 13. However, the composite behaviour under the compression is different. No softening trend is observed due to the densification resulting from material crushing together, leading to an increasing stiffer response. Both tests enable the characterisation of the damage beginning and failure threshold for the ultimate tensile and compression strengths. Additionally, it can be seen that, unlike the multi-site model, the one-site model amplifies the enhancement of composite behaviour.

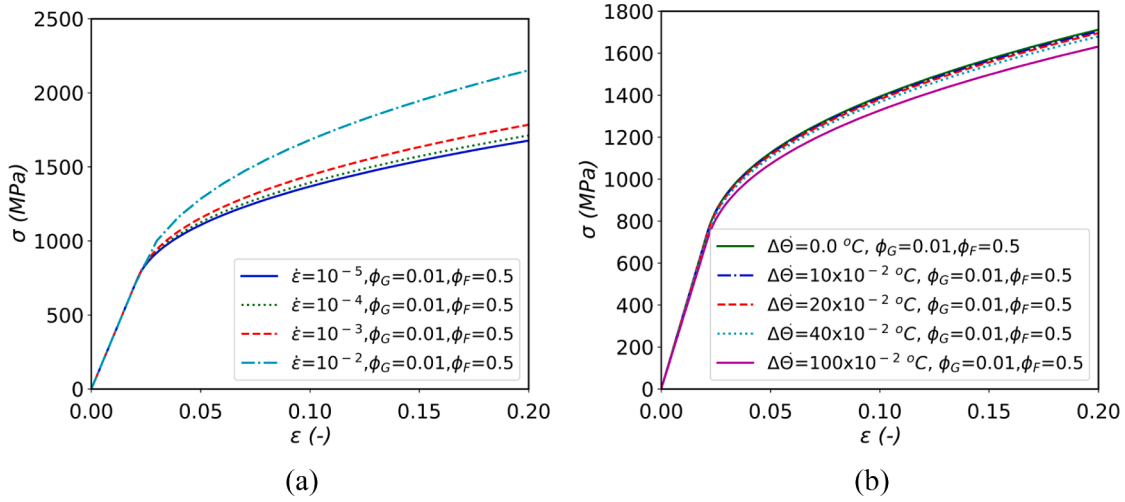

Fig. 9. Effective response of 3-phases composite under uniaxial loading using one-site model: (a) influence strain rate ($\dot{\varepsilon}$), and (b) influence of the temperature increment at $\dot{\varepsilon}$ = 10^{-4}.

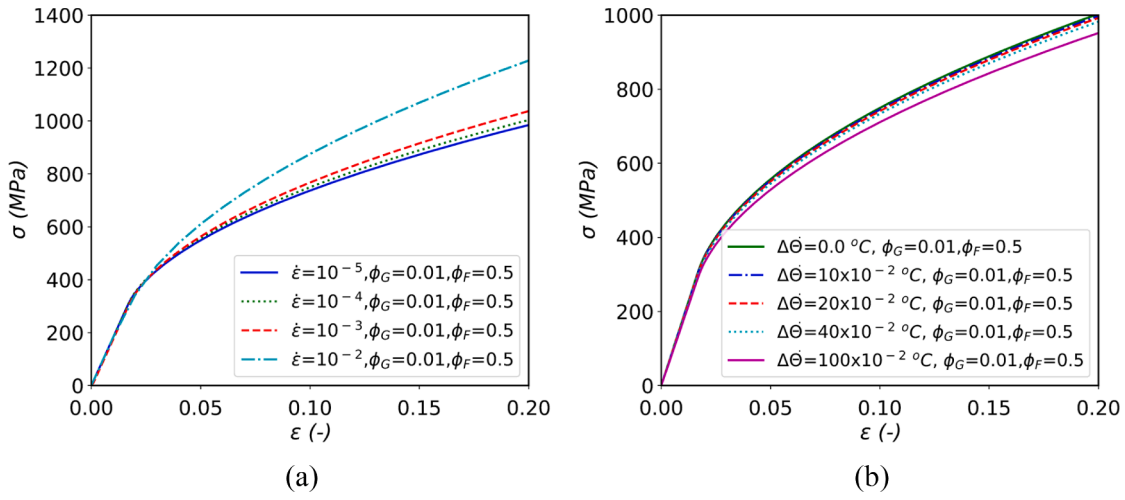

Fig. 10. Effective response of 3-phases composite under uniaxial loading using multi-site model: (a) influence strain rate ($\dot{\varepsilon}$), and (b) influence of the temperature increment at $\dot{\varepsilon}$ = 10^{-4}.

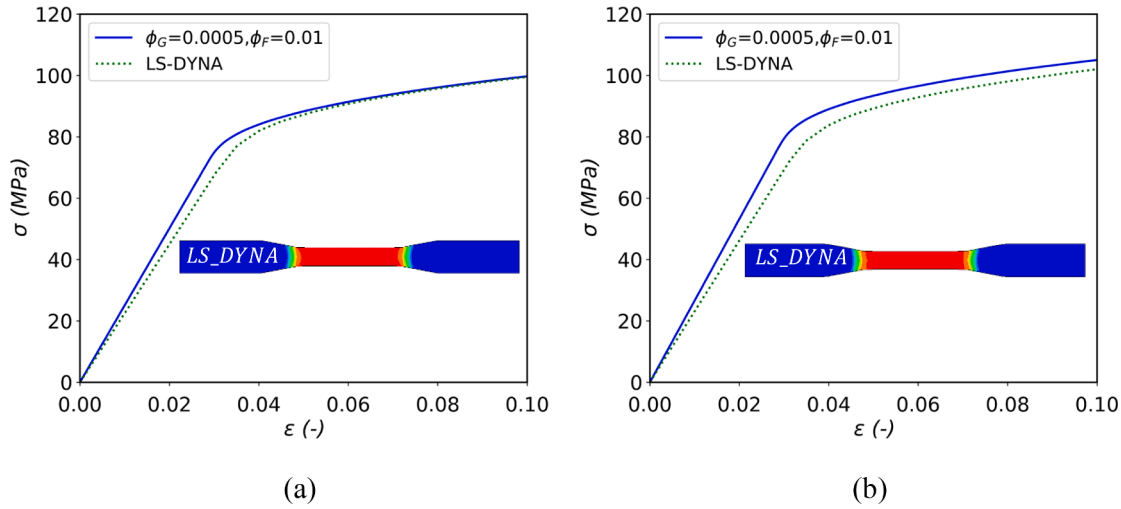

Fig. 11. Numerical versus analytical stress–strain behaviour of the 3-phases composite ($\phi_G = 0.0005$, $\phi_F = 0.01$) under tensile test: (a) one-site-model, and (b) multi-site model.

4.2.3. Crashworthiness and energy absorption application

A quarter of a symmetric crush tube of an automotive crash box is modelled to examine the crash performance. The geometry of the symmetric short crush tube depicted in Fig. 14 is created under LS-DYNA FE software [89,90]. The standard library 8-node solid elements are used for meshing purposes. The crushing load is applied on one side (upper) of the tube through a rigid wall moving at an initial impact velocity of 20 mph. The other (lower) side of the box is fully constrained. For symmetry constraints *BOUNDARY_SPC_SET command is used. Contact capabilities in LS-DYNA/EXPLICIT mainly*CONTACT AUTOMATIC SINGLE SURFACE are used to define the contact interactions between different parts of the model. The constitutive mechanical law

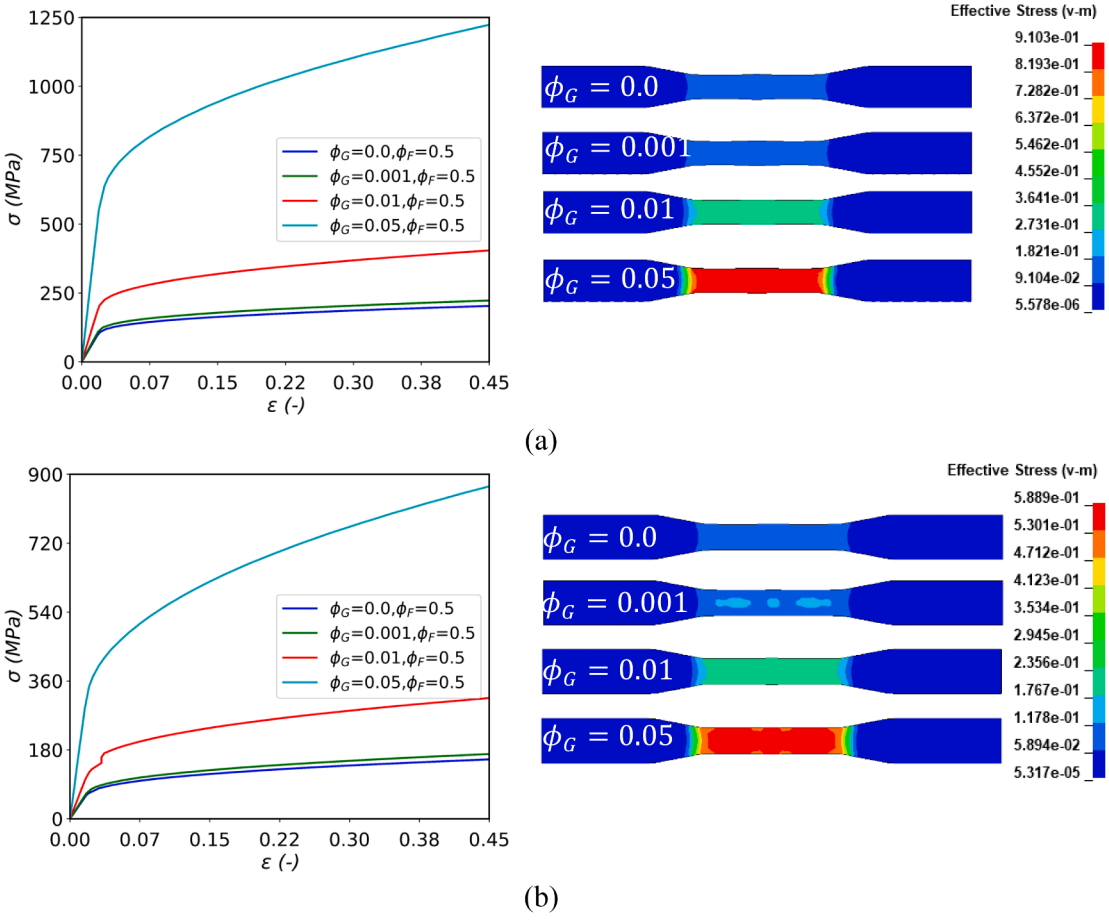

Fig. 12. Stress–strain behaviour of the 3-phases composite under tensile test: (a) one-site-model, and (b) multi-site model.

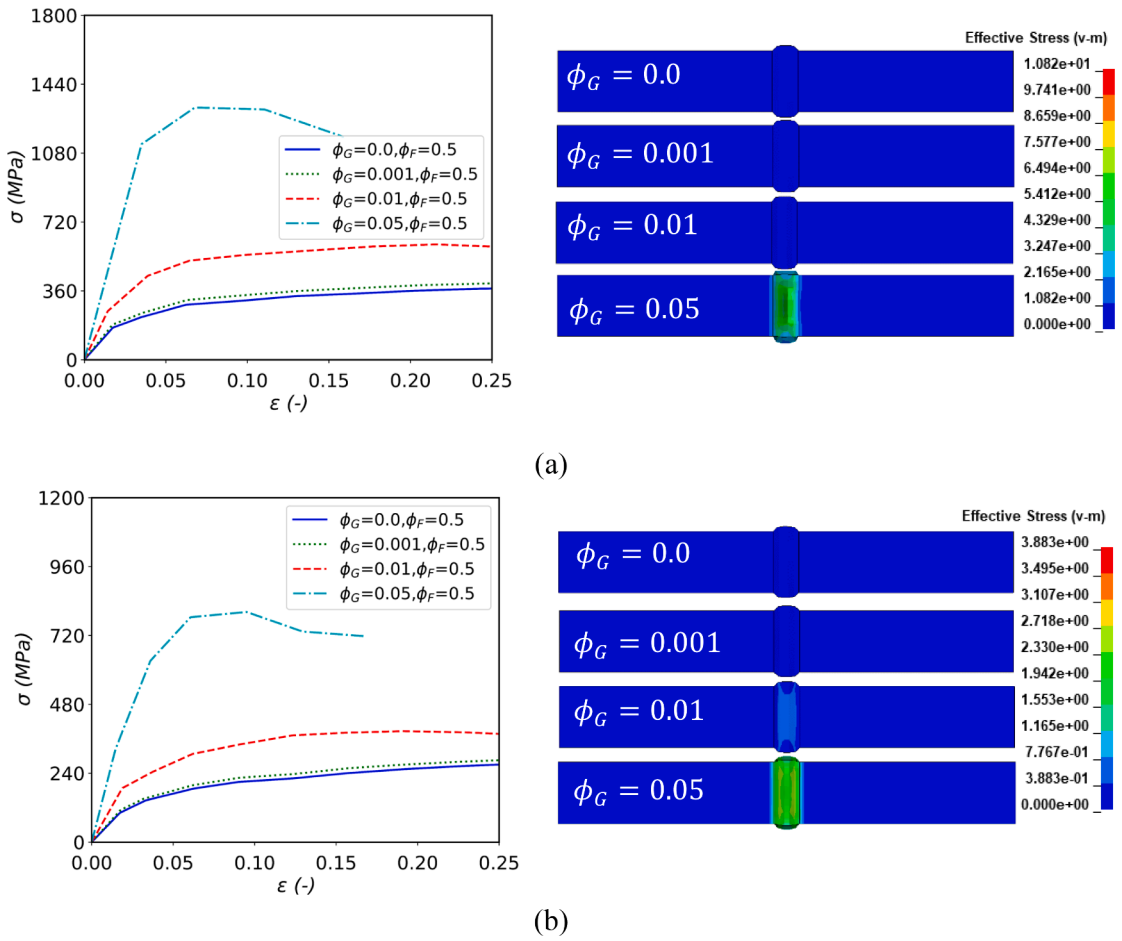

Fig. 13. Stress–strain behaviour of the 3-phases composite under compressive test: (a) one-site-model, and (b) multi-site model.

implemented in the crash box results from a user subroutine *MAT USER DEFINED MATERIAL MODELS. Failed continuum elements are removed using a damage-based element deletion.

Energy absorption is computed to determine the energy dissipation capability due to composite crushing. Energy absorption on the total work done is equal to the area under the force–displacement curve and evaluated as,

$$E_{abs} = \int F \mathrm{ds} \tag{49}$$

where F is the corresponding force on the structure and s is the impact distance. Energy absorption capability is also evaluated as per unit mass absorbed, i.e. specific energy absorption (SEA) and evaluated as,

$$\mathrm{SEA} = \frac{E_{abs}}{M} = \frac{E_{abs}}{\rho V} \tag{50}$$

where M is crushed mass, ρ is the composite material density, and V is the volume of the crush component.

The evolution of force–displacement and energy-displacement profiles obtained by the crushing of the tube specimens are depicted in the four diagrams of Fig. 15 grouped per modelling approach. At the beginning of crushing, the force–displacement curves in Fig. 15(a) and (b) show a linear segment of the loading controlled by the tube's elastic deformation. A considerable drop in the load is recorded after the peak force, indicating the starting of a post-crushing stage. Throughout this stage, most well-known damage mechanisms (e.g. matrix cracking, debonding, fibre micro buckling, delaminations, and fibre failure) interact, forming the load–displacement profile. Eventually, the composite tube reaches a densification stage, where the specimens cannot carry extra load, and the fixed boundary constraints contribute to the load-carrying capacity. For easy comparison, the data used are limited to 134 mm displacement before the densification stage. The energy absorbed profiles shown in Fig. 15(c) and (d) indicate a considerable enhancement in the composite energy absorption capability as the graphene volume fraction increases.

Fig. 16 compares steel versus 3-phases HGPNC composite responses. The peak crush force and the SEA obtained from a steel specimen are plotted against the 3-phases HGPNC composite. It can be seen that the respective peak crush force of both composite materials is much lower compared to that predicted by the steel. For the OS model, reduction percentages of ϕ_G = 0.0, 0.01 and 0.05 are 80.9%, 80.6% and 78%, respectively, whereas for MS model considering the same GNP volume fractions are 85.7%, 81.4% and 80.9%, respectively. However, the contribution of GNP is significant in terms of specific energy absorption SEA. Even in cases of the multi-site model, the higher the GNP volume fraction, the higher the SEA showing the contribution of the GNP in the enhancement of the energy absorption considering the strength-to-weight ratio.

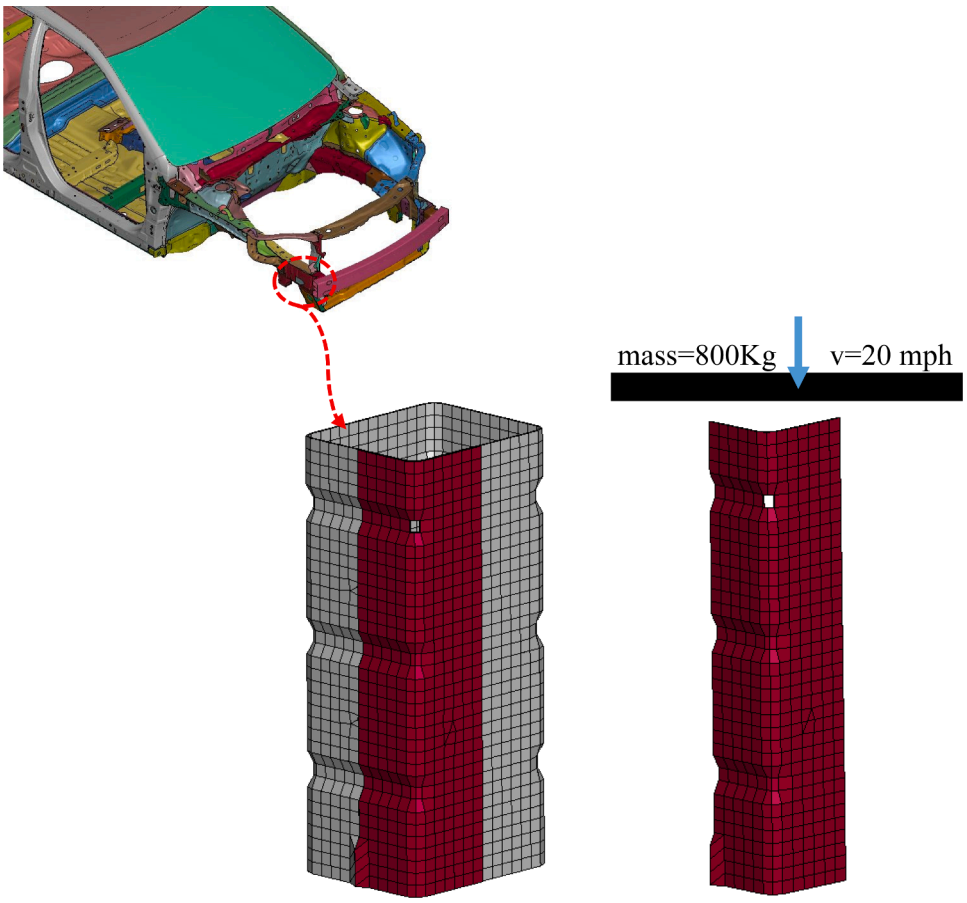

Fig. 14. Numerical model of symmetric crush tube of an automotive crash-box.

5. Conclusion

Multi-site (MS) modelling of the nonlinear elasto-viscoplastic response of 3-phases hierarchical fibres/graphene nanoplatelets-reinforced polymer matrix (HGPNC) composites has been analysed. Furthermore, the analysis of MS was compared with the traditional OS modelling. Generally, the analysis consists of modelling the 2-phases GPNC composite, whose effective properties are obtained from micro-mechanics formalism. Next, short glass fibres are embedded in the 2-phases composite to obtain the HGPNC 3-phases composite. Finally, different design parameters are analysed, including volume fraction, temperature, and strain rate.

Models have been validated and implemented as a UMAT subroutine in LS-DYNA®. Before utilising the models for crashworthiness application, numerical characterisation-based ASTM standard tests are performed in tensile and compression to determine material damage thresholds needed to indicate the failure onset of the simulated component. The comparison between analytical and FE tensile testing indicates good agreement between the results, revealing that implementing the stress integration algorithm developed and used for the UMAT is successful.

The crashworthiness of both models is then assessed for automotive components' response in a multiscale crashworthiness simulation. Results highlight the disparity between MS and OS approaches. When MS is considered, the simulation results for the FE macro-model indicate a reduction of the peak crush force (with percentages of 4.1% and 13% at $\phi_G = 0.01$ and 0.05, respectively) and energy absorption (37.2 % and 44.4% at $\phi_G = 0.01$ and 0.05, respectively) compared to the OS results, as the GNP volume fraction increases. In general, the volume fraction of GNP seems to significantly improve the specific energy absorption of the structure compared to the steel counterpart considering strength to weight ratio. Contrasting the OS model, the MS model results showed more discretion (decrease versus the OS) regarding material responses due to the interaction between neighbouring inclusions. Design-wise, MS modelling can be considered a safer approach to follow.

The current method is a coupling between fast and cheap analytical techniques and the computationally expensive numerical FE method. It represents a computational homogenisation model of two-scale homogenisation for the 3-phases composite and can be easily generalized to a multiscale homogenisation method applicable to a multi-phase polymeric matrix composite system of elastic or inelastic reinforcements. However, some limitations should be taken into consideration: the reinforced inclusions would be of the same shape and alignment, and convergence problems may be encountered. Although the MS approach has the advantage of dealing with the material's anisotropy through the morphological and topological textures of the microstructure, more computing time may be required over the OS approach to obtain results.

Future research may address conducting investigations and pursuing a suitable model for failure and fragmentation behaviour, e.g. mesh

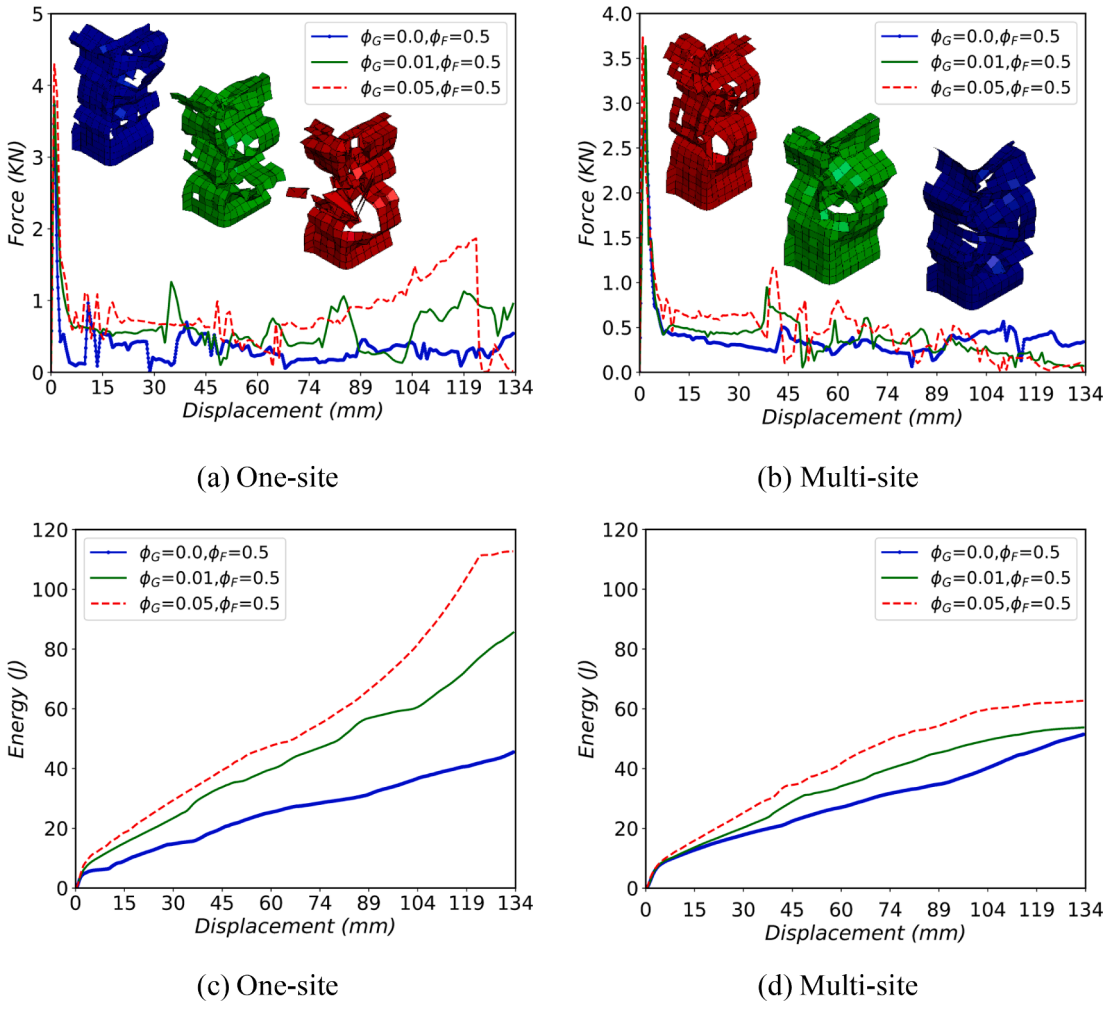

Fig. 15. Symmetric crush tube of 3-phases composite: (a) & (b) force versus displacement, and (c) & (d) energy absorption versus displacement.

splitting or user-defined element interface to define structural solid/shell elements. This model would be incorporated with the current UMAT model instead of elements just being distorted, overlapped, folded or deleted under large deformations when reaching a failure criterion. Furthermore, not only individual components and structures can be simulated but also as part of whole-vehicle models. For example, a whole-vehicle simulation model can be used to virtually "crash" the vehicle into a barrier and carry out crashing analyses. Finally, The use of artificial intelligence (AI) and machine learning (ML)-based approaches such as artificial neural networks (ANNs) could be employed in future work. Although applying such techniques for constitutive material modelling is recent and not fully explored, they could potentially overcome the computational time constraints.

CRediT authorship contribution statement

Ahmed Elmasry: Conceptualization, Data curation, Formal analysis, Investigation, Methodology, Resources, Software, Validation, Visualization, Writing – original draft, Writing – review & editing. **Wiyao Azoti:** Conceptualization , Methodology, Software, Writing – original draft, Writing – review & editing. **Ahmed Elmarakbi:** Supervision, Methodology, Resources, Software, Writing – review & editing.

Declaration of Competing Interest

The authors declare that they have no known competing financial interests or personal relationships that could have appeared to influence the work reported in this paper.

Data availability

The research codes are part of another ongoing research project.

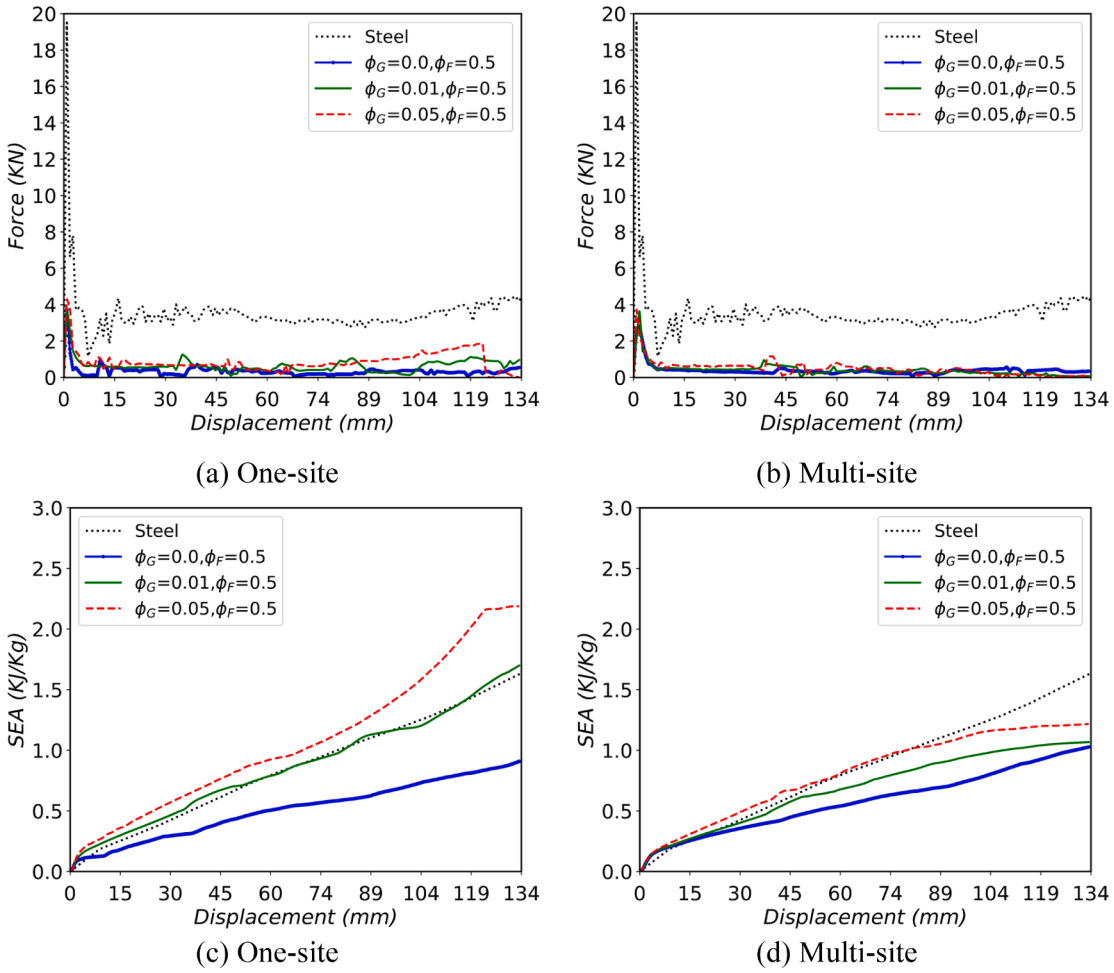

Fig. 16. Symmetric crush tube of steel versus 3-phases composite: (a) & (b) force versus displacement, and (c) & (d) specific energy absorption versus displacement.

Appendix A

To establish the integral relation of Eq. (15) between the local velocity gradient of the inhomogeneous medium and the kinematic boundary conditions:

Eq. (13) may be rewritten in another form,

$$\Lambda_{jl}u_l(r)+f_j(r)=0 \tag{A1}$$

where

$$\Lambda_{jl}=c^R_{ijkl}\partial_k\partial_l$$
$$f_j=\left[\delta c_{ijkl}(r)u_{l,k}(r)-\delta\beta_{ij}(r)\Delta\theta\right]_{,i} \tag{A2}$$

are, respectively, the Lame's operator and volume force. Equation (13) can be transformed into the integral equation by means of the Green tensor $G_{km}(r-r')$ for the infinite medium characterized by c^R. This Green tensor couples velocity components $u_l(r)$ at r with a rate of force $\dot{t}$ applied in the direction m at the position r'.

$$c^R_{ijkl}G_{lm,ki}(r-r')+\delta_{jm}\delta(r-r')=0 \tag{A3}$$

including the requirement: $G_{lm}\to 0$ when $r\to\infty$. The properties of the Dirac distribution $\delta(r-r')$ and the Kronecker symbol δ_{jm} imply

$$u_m(r)=\int_{V'}\delta_{mj}\delta(r-r')u_j(r')dV' \tag{A4}$$

and taking Eq. (A2) into account results in:

$$u_m(r)=-\int_{V'}c^R_{ijkl}G_{lm,ki}(r-r')u_j(r')dV' \tag{A5}$$

Using the property:

$$G_{lm,k}=\frac{\partial G_{lm}}{\partial r_k}=-\frac{\partial G_{lm}}{\partial r'_k}=-G_{lm,k} \tag{A6}$$

and, after integration by parts, integral (A5) becomes:

$$u_m(r) = -\int_{V'} c^R_{ijkl}\left[G_{lm,k'}u_j(r')\right]_{,i'}dV' + \int_{V'} c^R_{ijkl}\left[G_{lm}(r-r')u_{j,i}(r')\right]_{,k'}dV' - \int_{V'} c^R_{ijkl}G_{lm}(r-r')u_{j,ik}(r')dV' \tag{A7}$$

Making use of the divergence theorem, the first two volume integrals are transformed into surface integrals:

$$u_m(r) = -\int_{S'} c^R_{ijkl}G_{lm,k'}u_j(r')dS'_i + \int_{S'} c^R_{ijkl}G_{lm}(r-r')u_{j,i}(r')dS'_k - \int_{V'} c^R_{ijkl}G_{lm}(r-r')u_{j,ik}(r')dV' \tag{A8}$$

Considering the symmetry property:

$$c^R_{ijkl}G_{lm}(r-r')u_{j,ik}(r') = c^R_{ijkl}G_{mj}(r-r')u_{l,ik}(r') \tag{A9}$$

Now, using Eq. (13) yields:

$$c^R_{ijkl}G_{lm}(r-r')u_{j,ik}(r') = -G_{mj}(r-r')\left[\delta c_{ijkl}(r')u_{l,k}(r') - \delta\beta_{ij}(r')\Delta\theta\right]_{,i} \tag{A10}$$

thus, Eq. (A8).

$$u_m(r) = \quad -\int_{S'} c^R_{ijkl}G_{lm,k'}u_j(r')dS'_i + \int_{S'} c^R_{ijkl}G_{lm}(r-r')u_{j,i}(r')dS'_k + \int_{V'} G_{mj}(r-r')\left[\delta c_{ijkl}(r')u_{l,k}(r') - \delta\beta_{ij}(r')\Delta\theta\right]_{,i}dV' \tag{A11}$$

After an integration by parts, the last integral may be changed to a volume and a surface.
integrals and Eq. (A11) is replaced by.

$$u_m(r) = -\int_{S'} c^R_{ijkl}G_{lm,k'}(r-r')u_j(r')dS'_i + \int_{S'} c^R_{ijkl}G_{lm}(r-r')u_{j,i}(r')dS'_k + \int_{S'} G_{mj}(r-r')\left[\delta c_{ijkl}(r')u_{l,k}(r') - \delta\beta_{ij}(r')\Delta\theta\right]dS'_i - \int_{V'} G_{mj,i}(r-r')\left[\delta c_{ijkl}(r')u_{l,k}(r') - \delta\beta_{ij}(r')\Delta\theta\right]dV' \tag{A12}$$

The second and third surface integrals disappear because of Green's tensor property for $r\to\infty$. The first surface integral presents the solution to the homogeneous problem (homogeneous material of c^R_{ijkl} instantaneous tangent moduli which is submitted to the real boundary conditions). Defining this solution as $U^R_m = u^R_m(r)$ one may write:

$$u_m(r) = U^R_m + \int_{V'} G_{mj,i}(r-r')\left[\delta c_{ijkl}(r')u_{l,k}(r') - \delta\beta_{ij}(r')\Delta\theta\right]dV' \tag{A13}$$

The velocity gradient may now be calculated as,

$$G_{mn}(\mathbf{x}) = u_{m,n}(r) = U^R_{m,n} + \int_{V'} G_{mj,in}(r-r')\left[\delta c_{ijkl}(r')u_{l,k}(r') - \delta\beta_{ij}(r')\Delta\theta\right]dV' \tag{A14}$$

Solution of the general equation of heterogeneous inclusions to obtain Eq. (21):

Generally, the field $\boldsymbol{\varepsilon}(r)$ inside inclusions of any shape is not uniform. In that case, the exact solution of Eq. (16) requires numerical methods or approximation of $\boldsymbol{\varepsilon}(r)$ using a polynomial form [91]. In most real situations, it is reasonable to assume that $\boldsymbol{\varepsilon}(r)$ is quasi uniform inside the inclusions, so that the average value $\boldsymbol{\varepsilon}^I$, $\boldsymbol{\varepsilon}^J$, … etc of $\boldsymbol{\varepsilon}(r)$ inside the inclusions I , J, …etc may be obtained as follows:

From Eq. (16) in (19):

$$\varepsilon^I_{mn} = E^R_{mn} - \frac{1}{V_I}\int_{V_I}\int_{V}\Gamma_{mnij}(r-r')\left[\Delta C^I_{ijkl}\aleph^I(r)\boldsymbol{\varepsilon}_{kl}(r') - \Delta\beta^I_{ij}\aleph^I(r)\Delta\theta\right]\,\mathrm{d}V\,\mathrm{d}V' - \frac{1}{V_I}\int_{V_I}\int_{V}\Gamma_{mnij}(r-r')\left[\Delta C^J_{ijkl}\aleph^J(r)\boldsymbol{\varepsilon}_{kl}(r') - \Delta\beta^J_{ij}\aleph^J(r)\Delta\theta\right]\,\mathrm{d}V\,\mathrm{d}V' - \cdots etc \tag{A15}$$

To obtain $\boldsymbol{\varepsilon}^J$, from an analogous formula:

$$\boldsymbol{\varepsilon}^J = \frac{1}{V^J}\int_{V^J}\varepsilon^J_{mn}(r)dV \tag{A16}$$

$$\varepsilon^J_{mn} = E^R_{mn} - \frac{1}{V_J}\int_{V_J}\int_{V}\Gamma_{mnij}(r-r')\left[\Delta C^J_{ijkl}\aleph^J(r)\boldsymbol{\varepsilon}_{kl}(r') - \Delta\beta^J_{ij}\aleph^J(r)\Delta\theta\right]\mathrm{d}V\,\mathrm{d}V' - \frac{1}{V_J}\int_{V_J}\int_{V}\Gamma_{mnij}(r-r')\left[\Delta C^I_{ijkl}\aleph^I(r)\boldsymbol{\varepsilon}_{kl}(r') - \Delta\beta^I_{ij}\aleph^I(r)\Delta\theta\right]\,\mathrm{d}V\,\mathrm{d}V' - \cdots etc \tag{A17}$$

The exact solution of these equations is still very complex and difficult to deduce in general; an approximate solution can be obtained by replacing the deformations $\boldsymbol{\varepsilon}(r)$ integrals in Eq. (A15) and Eq. (A17) by their average value $\boldsymbol{\varepsilon}^I$, $\boldsymbol{\varepsilon}^J$, …etc in the inclusions I, J, …etc.

Thus Eq. (A15) becomes,

$$\varepsilon^I_{mn} = E^R_{mn} - \frac{1}{V_I}\int_{V_I}\int_{V_I}\Gamma_{mnij}(r-r')\left[\Delta C^I_{ijkl}\varepsilon^I_{kl}(r') - \Delta\beta^I_{ij}\Delta\theta\right]\,\mathrm{d}V\,\mathrm{d}V' - \frac{1}{V_I}\int_{V_I}\int_{V_J}\Gamma_{mnij}(r-r')\left[\Delta C^J_{ijkl}\varepsilon^J_{kl}(r') - \Delta\beta^J_{ij}\Delta\theta\right]\,\mathrm{d}V\,\mathrm{d}V' - \cdots etc \tag{A18}$$

and a similar expression for $\boldsymbol{\varepsilon}^J$ can be established.

By setting $\boldsymbol{T}^{II}_{mnij} = \frac{1}{V^I}\int_{V^I}\int_{V^I}\Gamma_{mnij}(r-r')dVdV'$ and $\boldsymbol{T}^{IJ}_{mnij} = \frac{1}{V^I}\int_{V^J}\int_{V^J}\Gamma_{mnij}(r-r')dVdV'$, the following linear system is obtained:

$$\varepsilon^{I}_{mn} = E^{R}_{mn} - \boldsymbol{T}^{II}_{mnij}\left[\Delta C^{I}_{ijkl}\varepsilon^{I}_{kl} - \Delta\beta^{I}_{ij}\Delta\theta\right] - \boldsymbol{T}^{IJ}_{mnij}\left[\Delta C^{J}_{ijkl}\varepsilon^{J}_{kl} - \Delta\beta^{J}_{ij}\Delta\theta\right]\,\mathrm{d}V\,\mathrm{d}V^{'} - \cdots etc$$

or

$$\boldsymbol{\varepsilon}^{I} = \boldsymbol{E}^{R} - \sum_{J}\boldsymbol{T}^{IJ} : \left[\Delta\boldsymbol{c}^{J} : \boldsymbol{\varepsilon}^{J} - \Delta\boldsymbol{\beta}^{J}\Delta\theta\right] \tag{A19}$$

Similarly by setting $\boldsymbol{T}^{JJ}_{mnij} = \frac{1}{V^{J}}\int_{V^{J}}\int_{V^{J}}\Gamma_{mnij}(\boldsymbol{r}-\boldsymbol{r}^{'})dVdV^{'}$ and $\boldsymbol{T}^{IJ}_{mnij} = \frac{1}{V^{J}}\int_{V^{J}}\int_{V^{J}}\Gamma_{mnij}(\boldsymbol{r}-\boldsymbol{r}^{'})dVdV^{'}$, results in:

$$\varepsilon^{J}_{mn} = E^{R}_{mn} - \boldsymbol{T}^{IJ}_{mnij}\left[\Delta C^{J}_{ijkl}\varepsilon^{J}_{kl} - \Delta\beta^{J}_{ij}\Delta\theta\right] - \boldsymbol{T}^{IJ}_{mnij}\left[\Delta C^{I}_{ijkl}\varepsilon^{I}_{kl} - \Delta\beta^{I}_{ij}\Delta\theta\right]\,\mathrm{d}V\,\mathrm{d}V^{'} - \cdots etc$$

or

$$\boldsymbol{\varepsilon}^{J} = \boldsymbol{E}^{R} - \sum_{I}\boldsymbol{T}^{IJ} : \left[\Delta\boldsymbol{c}^{I} : \boldsymbol{\varepsilon}^{I} - \Delta\boldsymbol{\beta}^{I}\Delta\theta\right] \tag{A20}$$

General expressions and numerical quadrature for approximate computation of T^{II} and T^{IJ}:

Considering ellipsoidal-shaped inclusion with semi-axis (a, b, c), the following expressions based on the Fourier transform $\overline{\boldsymbol{G}}$ of the Green tensor $\boldsymbol{G}$ could be provided [32]:

$$\boldsymbol{T}^{II}_{mnij} = \frac{1}{4\pi}\int_{0-0}^{\pi}\int_{\varphi-0}^{2\pi}\chi_n\chi_j\boldsymbol{\kappa}^{2}\overline{G}_{mi}(\xi)\sin\theta d\varphi d\theta \tag{A21}$$

and,

$$\boldsymbol{T}^{IJ}_{mnij} = \frac{9}{8\pi^{3}}V_J\int_{\theta=0}^{\pi}\int_{\varphi=0}^{2\pi}w_n w_j\boldsymbol{\kappa}^{2}\overline{G}_{mj}(\xi)\sin\theta F(\theta,\varphi)d\varphi d\theta \tag{A22}$$

where $\boldsymbol{\chi} = \left[\sin\theta\cos\varphi, \frac{a}{b}\sin\theta\sin\varphi, \frac{a}{c}\cos\theta\right]$ and $\boldsymbol{W} = [\sin\theta\cos\varphi, \sin\theta\sin\varphi, \cos\theta]$ in Eqs. (A21) and (A22), respectively. Variables θ and φ are the directional cosines while $\boldsymbol{\xi}$ is defined by $\xi_i = \boldsymbol{\kappa}\chi_i, \boldsymbol{\kappa}^{2}\overline{G}_{jk}(\boldsymbol{\xi}) = \left(c^{R}_{ijkl}\chi_i\chi_l\right)^{-1}$ and $F(\theta,\varphi)$ is a function of the inclusions' morphological and topological textures.

References

[1] Dericiler K, Aliyeva N, Sadeghi HM, Sas HS, Menceloglu YZ, Okan BS. Chapter 30 - Graphene in automotive parts. In: Song H, Nguyen TA, Yasin G, Singh NB, Gupta RK, editors. Nanotechnology in the automotive Industry. Elsevier; 2022. p. 623–51.

[2] Sun X, Huang C, Wang L, Liang L, Cheng Y, Fei W, et al. Recent progress in graphene/polymer nanocomposites. Adv Mater 2021;33.

[3] Mohan VB, Lau K-T, Hui D, Bhattacharyya D. Graphene-based materials and their composites: a review on production, applications and product limitations. Compos B Eng 2018;142:200–20.

[4] Ravishankar B, Nayak SK, Kader MA. Hybrid composites for automotive applications – a review. J Reinf Plast Compos 2019;38(18):835–45.

[5] Fentahun MA, Savaş MA. Materials used in automotive manufacture and material selection using Ashby charts. Int J Mater Eng 2018;8(3):40–54.

[6] Patel M, Pardhi B, Chopara S, Pal M. Lightweight composite materials for automotive - a review. Int Res J Eng Technol (IRJET) 2018;5(11):41–7.

[7] Ghassemieh E. Materials in automotive application, state of the art and prospects. In: Chiaberge M, editor. New trends and developments in automotive industry. InTech; 2011. p. 365–94.

[8] Mahieux CA. Environmental Degradation of Industrial Composites. p. 1–16.

[9] Hu K, Kulkarni DD, Choi I, Tsukruk VV. Graphene-polymer nanocomposites for structural and functional applications. Prog Polym Sci 2014;39(11):1934–72.

[10] Liu B, Pavlou C, Wang Z, Cang Y, Galiotis C, Fytas G. Determination of the elastic moduli of CVD graphene by probing graphene/polymer Bragg stacks. 2D Materials 2021;8(3):035040.

[11] Thomas S, Ajith KM, Lee SU, Valsakumar MC. Assessment of the mechanical properties of monolayer graphene using the energy and strainf luctuation methods. RSC Adv 2018;8(48):27283–92.

[12] Cao K, Feng S, Han Y, Gao L, Ly TH, Xu Z, et al. Elastic straining of free-standing monolayer graphene. Nat Commun 2020;11(284).

[13] Elmarakbi A, Azoti W. Mechanical prediction of graphene-based polymer nanocomposites for energy-efficient and safe vehicles. In: Sciarra FMd, Russo P, editors. Experimental characterization, predictive mechanical and thermal modeling of nanostructures and their polymer composites. Elsevier; 2018. p. 159–77.

[14] Li A, Zhang C, Zhang Y-F. Thermal conductivity of graphene-polymer composites: mechanisms, properties, and applications. Polymers 2017;9(9):1–17.

[15] Li W, Dichiara A, Bai J. Carbon nanotube–graphene nanoplatelet hybrids as high-performance multifunctional reinforcements in epoxy composites. Compos Sci Technol 2013;74:221–7.

[16] Elmarakbi A, Azoti W. State of the art on graphene lightweighting nanocomposites for automotive applications. In: Sciarra FMD, Russo P, editors. Experimental characterization, predictive mechanical and thermal modeling of nanostructures and their polymer composites. Elsevier; 2018. p. 1–23.

[17] Martorana B, Elmarakbi A, Veca A, Fondacaro D, Lambertini VG. Graphene-based materials: opportunities for multifunctional lightweight structures in automotive sector. Nanotech; 2015.

[18] Izzaty N, Ilyas Sastra HY. The implementation of graphene composites for automotive: an industrial perspective 2019;536(1):012133.

[19] Kumar V, Sengupta S, Raj B. Materials modelling and design: an introduction. In: Kumar V, Sengupta S, Raj B, editors. Frontiers in materials modelling and design. Berlin Heidelberg: Springer-Verlag; 1998. p. 3–7.

[20] Vieira AFC, editor. Material modelling: applications, challenges and research. Nova Science Publishers; 2017.

[21] Ye L, editor. Recent advances in structural integrity analysis: proceedings of the international congress (APCF/SIF-2014). Woodhead Publishing; 2015.

[22] Guo ZX, editor. Multiscale materials modelling: fundamentals and applications. Elsevier Science; 2007.

[23] Elmasry A, Azoti W, Elmarakbi M, Elmarakbi A. Interaction modelling of the thermomechanical behaviour of spatially-oriented graphene platelets (GPLs) reinforced polymer matrix. Int J Solids Struct 2021;232:111183.

[24] Elmasry A, Azoti W, El-Safty SA, Elmarakbi A. A comparative review of multiscale models for effective properties of nano- and micro-composites. Prog Mater Sci 2023;132:101022.

[25] Fassi-Fehri O, Hihi A, Berveiller M. Multiple site self consistent. Int J Eng Sci 1989; 27(5):495–502.

[26] Ju JW, Chen TM. Micromechanics and effective moduli of elastic composites containing randomly dispersed ellipsoidal inhomogeneities. Acta Mechanica 1994; 103:103–21.

[27] Ju JW, Chen TM. Effective elastic moduli of two-phase composites containing randomly dispersed spherical inhomogeneities. Acta Mechanica 1994;103:123–44.

[28] Ju J, Tseng K. Effective elastoplastic behavior of two-phase metal matrix composites: micromechanics and computational algorithms. In: Voyiadjis GZ, Ju J, editors. Studies in Applied Mechanics, vol. 41. Elsevier; 1994. p. 121–41.

[29] Ju J, Sun L. Effective elastoplastic behavior of metal matrix composites containing randomly located aligned spheroidal inhomogeneities. Part I: micromechanics-based formulation. Int J Solids Struct 2001;38:183–201.

[30] Sun LZ, Ju JW. Effective elastoplastic behavior of metal matrix composites containing randomly located aligned spheroidal inhomogeneities. Part II: Applications. Int J Solids Struct 2001;38:203–25.

[31] Kpobie W, Khlifa SB, Bonfoh N, Fendler M, Lipinski P. Multi-site micromechanical modelling of thermo-elastic properties of heterogeneous materials. Compos Struct 2012;94(6):2068–77.

[32] Azoti W, Koutsawa Y, Tchalla A, Makradi A, Belouettar S. Micromechanics-based multi-site modeling of elastoplastic behavior of composite materials. Int J Solids Struct 2015;59:198–207.

[33] Geers MGD, Kouznetsova VG, Matouš K, Yvonnet J. Homogenization methods and multiscale modeling: nonlinear problems. In: Stein E, Borst Rd, Hughes TJR, editors. Encyclopedia of computational mechanics. 2nd ed. New York: John Wiley & Sons, Ltd; 2017. p. 1–34.

[34] Borst R, Ramm E, editors. Multiscale methods in computational mechanics: progress and accomplishments. 1st ed., 55. Heidelberg: Springer; 2011.

[35] Pineda EJ, Bednarcyk BA, Waas AM, Arnold SM. Progressive failure of a unidirectional fiber-reinforced composite using the method of cells: discretization objective computational results. Int J Solids Struct 2013;50(9):1203–16.

[36] Kaleel I, Petrolo M, Carrera E, Waas AM. Computationally efficient concurrent multiscale framework for the linear analysis of composite structures. AIAA J 2019; 57(9):4019–28.

[37] Sun Y, Hu Y, Liu M. Elasto-plastic behavior of graphene reinforced nanocomposites with hard/soft interface effects. Mater Des 2021;199:109421.
[38] Tsiamaki AS, Anifantis NK. Finite element simulation of the thermomechanical response of graphene reinforced nanocomposites. In: 5th International conference of engineering against failure (ICEAF-V 2018); 2018.
[39] Tsiamaki A, Anifantis N. Simulation of the thermomechanical behavior of graphene/PMMA nanocomposites via continuum mechanics. Int J Struct Integrity 2019;11(5):655–69.
[40] Sandu T, Gologanu M, Voicu R, Boldeiu G, Moagar-Poladian V. Modeling issues regarding thermal conductivity of graphene-based nanocomposites. Romanian J Inf Sci Technol 2018;21(1):82–92.
[41] Yang S-Y, Lin W-N, Huang Y-L, Tien H-W, Wang J-Y, Ma C-C-M, et al. Synergetic effects of graphene platelets and carbon nanotubes on the mechanical and thermal properties of epoxy composites. Carbon 2011;49(3):793–803.
[42] Rahman MH, Mitra S, Motalab M, Bose P. Investigation on the mechanical properties and fracture phenomenon of silicon doped graphene by molecular dynamics simulation. RSC Adv 2020;10(52):31318–32.
[43] Zhao X, Zhang Q, Chen D, Lu P. Enhanced mechanical properties of graphene-based poly(vinyl alcohol) composites. Macromolecules 2010:2357–63.
[44] Zhou X, Zhang X, Xu S, Wu S, Liu Q, Fan Z. Evaluation of thermo-mechanical properties of graphene/carbon-nanotubes modified asphalt with molecular simulation. Mol Simul 2017;43(4):312–9.
[45] Pinto F, Carotenuto G, Meo M. Preparation and thermomechanical characterisation of graphene nanoplatelets/ low-density polyethylene composites. J Thermoplast Compos Mater 2013;28(6):745–61.
[46] Wang E, Dong Y, Islam MZ, Yu L, Liu F, Chen S, et al. Effect of graphene oxide-carbon nanotube hybrid filler on the mechanical property and thermal response speed of shape memory epoxy composites. Compos Sci Technol 2019;169:209–16.
[47] Tarawneh MA, Saraireh SA, Chen RS, Ahmad SH, Al-Tarawni MAM, Al-Tweissi M, et al. Mechanical, thermal, and conductivity performances of novel thermoplastic natural rubber/graphene nanoplates/polyaniline composites. J Appl Mater Sci 2020;137(28):48873.
[48] Georgantzinos SK, Giannopoulos GI, Anifantis NK. Coupled thermomechanical behavior of graphene using the spring-based finite element. J Appl Phys 2016;120 (1):014305.
[49] Li Z, Zheng J, Zhang Z. Thermal nonlinear performance of the porous metal cylinders with composite graphene nanofiller reinforcement encased in elastic mediums. Int J Mech Sci 2020;181:105698.
[50] Miled B, Doghri I, Brassart L, Delannay L. Micromechanical modeling of coupled viscoelastic–viscoplastic composites based on an incrementally affine formulation. Int J Solids Struct 2013;50(10):1755–69.
[51] Isaac CW, Ezekwem C. A review of the crashworthiness performance of energy absorbing composite structure within the context of materials, manufacturing and maintenance for sustainability. Compos Struct 2021;257:113081.
[52] Phillips R. Crystals, defects and microstructures: modeling across scales. Cambridge University Press; 2001. p. 66–9.
[53] Qin Q-H. Green's function and boundary elements of multifield materials. Elsevier Science; 2010.
[54] Eshelby JD. The determination of the elastic field of an ellipsoidal inclusion, and related problems. Proc Math Phys Eng Sci 1957;241(1226):376–96.
[55] Korringa J. Theory of elastic constants of heterogeneous media. J Math Phys 1973; 14(4):509–13.
[56] Zeller R, Dederichs PH. Elastic constants of polycrystals. physica status solidi (b) 1973;55(2):831–42.
[57] Kröner E. Zur Klassichen Theorie Statistisch aufgebauter Festkörper. Int J Eng Sci 1973;11:171–91.
[58] Kröner E. Bounds for effective elastic moduli of disordered materials. J Mech Phys Solids 1977;25(2):137–55.
[59] Ferrari M. Asymmetry and the high concentration limit of the Mori-Tanaka effective medium theory. Mech Mater 1991;11:251–6.
[60] Miled B, Doghri I, Delannay L. Coupled viscoelastic–viscoplastic modeling of homogeneous and isotropic polymers: numerical algorithm and analytical solutions. Comput Methods Appl Mech Eng 2011;200(47–48):3381–94.
[61] Doghri I. Mechanics of solids: linear, nonlinear, analytical and computational aspects. Springer; 2000.
[62] Norton FH. The creep of steel at high temperatures. New York: McGraw-Hill; 1929.
[63] Odqvist FKG. Plasticity theory with applications. Royal Swedish Acad Eng Sci 1933.
[64] Odqvist F. Historical survey of the development of creep mechanics from its beginnings in the last century to 1970. In: Panter ARS, Hayhurst DR, editors. Creep in structures, 3rd IUTAM symposium. Leicester: Springer-Verlag; 1980. p. 1–12.
[65] Jirasek M, Bazant ZP. Inelastic analysis of structures. Wiley; 2002. p. 541–54.
[66] Chaboche JL, Nouailhas D. A unified constitutive model for cyclic viscoplasticity and its applications to various stainless steels. J Eng Mater Technol 1989;111: 424–30.
[67] Perzyna P. The constitutive equations for rate sensitive plastic materials. Q Appl Math 1963;20(4):321–32.
[68] Perzyna P. Fundamental problems in viscoplasticity. In: Chernyi G, Dryden H, Germain P, Howarth L, Olszak W, Prager W, Probstein R, Ziegler H, editors. Advances in applied mechanics, vol. 9. Elsevier; 1966. p. 243–377.
[69] Perzyna P. Thermodynamic theory of viscoplasticity. In: Yih C, editor. Advances in applied mechanics, vol. 11. Elsevier; 1971. p. 313–54.
[70] Doghri I, Adam L. Bilger N. Mean-field homogenization of elasto-viscoplastic composites based on a general incrementally affine linearization method. Int J Plast 2010;26(2):219–38.
[71] Livermore Software Technology Corporation LSTC, LS-DYNA, Keyword User's Manual, 2022.
[72] Chandra Y, Scarpa F, Adhikari S, Zhang J, Flores ES, Peng H-X. Pullout strength of graphene and carbon nanotube/epoxy composites. Compos B Eng 2016;102:1–8.
[73] Shi Z, Li X-F, Bai H, Xu W-W, Yang S-Y, Lu Y, et al. Influence of microstructural features on thermal expansion coefficient in graphene/epoxy composites. Heliyon 2016;2(3):e00094.
[74] Rafiee MA, Rafiee J, Wang Z, Song H, Yu Z-Z, Koratkar N. Enhanced mechanical properties of nanocomposites at low graphene content. ACS Nano 2009;3(12): 3884–90.
[75] Zeng X, Yu S, Sun R, Xu J, Wong C-P. Effect of functionalized multiwalled carbon nanotubes on the coefficient of thermal expansion of bismaleimide-triazine resins (BT resins). In: 2015 IEEE 65th Electronic Components and Technology Conference (ECTC); 2015.
[76] Deng L, Young RJ, Kinloch IA, Sun R, Zhang G, Noe L, et al. Coefficient of thermal expansion of carbon nanotubes measured by Raman spectroscopy. Appl Phys Lett 2014;104(5):051907.
[77] Davis J, editor. Tensile testing. 2nd ed. Ohio: ASM International; 2004. p. 13–31.
[78] William J, Callister D, Rethwisch DG. Materials science and engineering: an introduction. Wiley; 2014.
[79] Azoti WL, Elmarakbi A. Multiscale modelling of graphene platelets-based nanocomposite materials. Compos Struct 2017;168:313–21.
[80] Azoti W, Elmarakbi A. Constitutive modelling of ductile damage matrix reinforced by platelets-like particles with imperfect interfaces: application to graphene polymer nanocomposite materials. Compos B Eng 2017;113:55–64.
[81] Azoti W, Elmarakbi A. A multiscale approach for the nonlinear mechanical response of 3-phases fiber reinforced graphene nanoplatelets polymer composite materials. Macromol Theory Simul 2019;28(4):1900011.
[82] Jiang J-W, Wang J-S, Li B. Thermal expansion in single-walled carbon nanotubes and graphene Nonequilibrium Green's function approach. Phys Rev B 2009;80(20): 205429.
[83] Yoon D, Son Y-W, Cheong H. Negative thermal expansion coefficient of graphene measured by Raman spectroscopy. Nano Lett 2011:3227–31.
[84] Jean F, Zhou T, Blanc N, Felici R, Coraux J, Renaud G. Effect of preparation on the commensurabilities and thermal expansion of graphene on Ir(111) between 10 and 1300 K. Phys Rev B 2013;88(16):165406.
[85] Standard Test Methods for Tension Testing of Metallic Materials [Metric] E 8M – 04. ASTM International.
[86] Standard Test Method for Tensile Properties of Plastics D638 – 10. ASTM International.
[87] Tensile Properties of Polymer Matrix Composite Materials D3039/D3039M – 14. ASTM International.
[88] Standard Test Method for Compressive Properties of Rigid Plastics D695. ASTM international.
[89] Reid J. Available from: https://www.dynaexamples.com/introduction/intro-by-j.-reid/symtube. Livermore Software Technology Corporation LSTC [Online].
[90] Reid J. Available from: https://www.dynaexamples.com/introduction/intro-by-j.-reid/crashbox. Livermore Software Technology Corporation LSTC [Online].
[91] Moschovidis ZA, Mura T. Two-ellipsoidal inhomogeneities by the equivalent inclusion method. J Appl Mech 1975;42(4):847–52.